Supporting Information

Laser-Induced Surface Hydroxylation of Nickel Oxide Boosting Monolayer Assembly for High-Performance Perovskite Solar Modules

Zheng Lv,[ab] Guozhen Liu,*[a] Zhiyong Wang,[ad] Yilin Gao,[ae] Muge Xu,[a] Lin Yang,[a] Ziyang Tian,[a] Yinjuan Zhang,[a] Guanghao Zhou,[a] Bo Xu,[a] Zicheng Liu,[ab] Guohao Dai,[a] Wei Lu,[a] Pengfei Wang,[ab] Jiazhen Wei,[a] Qingshun Dong,[c] Jiming Bian,[b] and Yantao Shi*[a]

[a] State Key Laboratory of Fine Chemicals, School of Chemistry, Frontier Science Center for Smart Materials, Dalian University of Technology, Dalian 116024, China

E-mail: gzliu@dlut.edu.cn, shiyantao@dlut.edu.cn

[b] Key Laboratory of Materials Modification by Laser, Ion and Electron Beams (Ministry of Education), School of Physics, Dalian University of Technology, Dalian 116024, China

[c] State Key Laboratory of Chemical Reaction Dynamics, Dalian Institute of Chemical Physics, Chinese Academy of Sciences, Dalian 116023, China

[d] State Key Laboratory of High-performance Precision Manufacturing, Dalian University of Technology, Dalian 116024, China

[e] School of Integrated Circuits, Dalian University of Technology, Dalian 116024, China

Experimental Section

Materials

All chemicals were purchased and used directly without further purification. Formamidine iodide (FAI, 99.5%) was gained from Greatcell Solar Materials Pty Ltd. Methylammonium iodide (MAI, 99.5%), methylammonium chloride (MACl, 99.5%), cesium iodide (CsI, 99.999%), phenyl-C_{61}-butyric acid methyl ester ($PC_{61}BM$, 99.9%), C_{60} (99.5%), Bathocuproine (BCP, 96%), and piperazinium diiodide (PDI, 99.5%)were purchased from Xi'an Yuri Solar Co., Ltd. PbI_2 (99.999%) was purchased from Advanced Election Technology Co. Ltd. Anhydrous dimethyl sulfoxide (DMSO), N,N-Dimethylformamide (DMF), N-Methyl-2-Pyrrolidinone (NMP, 99.5%), isopropyl alcohol (IPA, 99.5%) and chlorobenzene (CB, 99.8%) were all purchased from Sigma Aldrich. (4-(3,6-Dimethyl-9H-carbazole-9-yl)butyl) phosphonic acid (Me-4PACz, 99%) was purchased from TCI. polymethyl methacrylate (PMMA) were obtained from Sigma Aldrich Chemical Company Limited.

Fabrication of Large-area PSMs

First, the FTO substrates (10 cm × 10 cm) were laser-scribed using a 523 nm green laser to form the P1 line with width of 45 μm, delineating 11 sub-FTO regions on the substrate. Then the FTO substrates were cleaned sequentially using deionized water, ethanol and isopropanol for 20 mins in ultrasonic cleaner. After drying, all substrates transferred to magnetron sputtering chamber for deposition. The metal Ni target was selected as the Ni source. Pre-sputtering 120 s at DC power 80 W in Ar atmosphere to remove impurities on Ni target surface. Subsequently, a NiO_x film was deposited on FTO by sputtering for 500 s with 100 W DC power under room temperature. The atmosphere of the chamber remained at 3 Pa pressure, and Ar and O_2 fluxes rates were kept at 93 and 7 sccm, respectively. For the laser treatment, as-sputtered NiO_x films were irradiated by a 1064 nm nanosecond laser (Han's Laser Technology Industry Group Co., Ltd.) with an energy density of 32 mJ cm^{-2}. Then annealed the NiO_x film at room temperature

for 300 °C for 40 mins. Subsequently, the Me-4PACz solution was blade-coated onto NiO_x substrates at a speed of 10 mm s^{-1} and a coating gap of 200 μm, followed by annealing at 100 °C for 5 mins. Dissolving 557.8 mg PbI_2, 13.2 mg MACl, 24.7 mg CsI, 182.6 mg FAI in a 9:1 (v/v) DMF:NMP solvent mixture to obtain perovskite precursor. In an ambient atmosphere with temperature of 25 °C and a relative humidity of 20%-25% RH, the perovskite solution was first blade-coated onto the HTLs at a speed of 10 mm s^{-1} and a coating gap of 200 μm. The wet perovskite film is then transferred to a vacuum crystallization chamber at 3.0 Pa for 1 min, followed by annealing in air at 110 °C for 30 mins. Subsequently, C_{60} (25 nm) and BCP (5 nm) were sequentially deposited via thermal evaporation. After BCP deposition, the sample was laser-scribed to form the 37 μm wide P2 line using the aforementioned device. After that, the solar cell assembly was completed by thermally evaporating Cu (150 nm), followed by laser scribing to form the 37 μm wide P3 line. Finally, 11 subcells were connected to form a large area module with the aperture area of 65 cm^2.

Fabrication of Small-area PSCs

The purchased FTO substrates were cleaned sequentially using deionized water, ethanol and isopropanol for 20 mins in ultrasonic cleaner. After drying, the sputtered NiO_x films were prepared using the aforementioned method and subjected to laser irradiation. Then, the NiO_x film was transferred to a N_2 glovebox. Me-4PACz solution (0.5 mg mL^{-1} in IPA) was then spin-coated at 3000 rpm for 30 s, followed by annealing at 100 °C for 5 mins. For perovskite films, $Cs_{0.05}FA_{0.85}MA_{0.1}PbI_3$ solution with 1.5 M concentration was prepared by stoichiometrically mixing CsI, FAI, MAI and PbI_2 in a 4:1 (v/v) DMF:DMSO solvent mixture. Additives of 10 mol% excess PbI_2 and 20 mol% MACl were incorporated into the precursor to enhance crystallization. The perovskite precursor (90 μL) was spin-coated at 5000 rpm for 50 s with an acceleration of 2000 rpm s^{-1}. 160 μL of CB was dropped onto the film at 15 s before the end of the spin-coating process, followed by immediate annealing at 100 °C for 30 mins. After cooling,

the PDI (1 mg mL^{-1} in IPA) was spin-coated at 5000 rpm for 30 s onto the perovskite layer, and annealing at 100 °C for 10 mins. Subsequently, $PC_{61}BM$ (20 mg mL^{-1} in CB) and BCP (1 mg mL^{-1} in IPA) were separately spin-coated onto the perovskite layer at 1500 rpm for 30 s and 5000 rpm for 30 s, respectively. The film was then annealed at 60 °C for 5 mins. Under vacuum conditions (< 8×10^{-4} Pa), a 110 nm thick Ag electrode was thermally evaporated to finalize the device.

Characterization

The surface and cross-section morphologies of the thin films were observed using a field-emission SEM (JSM-7610F Plus, Hitachi, Japan). The crystallinity of perovskites films was tested by X-Ray diffractometer (XRD, D8 ADVANCE, Bruker, Germany). The GIWAXS measurements of perovskite films were performed at the BL14B1 beamline of the Shanghai Synchrotron Radiation Facility. Ultraviolet-visible (UV-vis) absorption and transmission spectrum tested by UV-vis spectrophotometer (Shimadzu, UV-3600 Plus, Japan). Fourier-transform infrared (FTIR) spectroscopy was conducted using an FT/IR-6700 (Thermo Fisher, USA) instrument. The XPS and ultraviolet photoelectron spectroscopy (UPS) measurements were tested by X-ray photoelectron spectrometer (ESCALAB250Xi, Thermo Fisher, USA). Kelvin Probe Force Microscopy (KPFM) and atomic force microscopy (AFM) measurements were performed with a Bruker Dimension Icon system. The wettability images were tested by an optical contact angle meter (Dataphysics, OCA50, Germany). The micelle particle size of the SAM solution was measured using a Nanoparticle size and zeta potential analyzer (Nano-ZS90, Malvern, U.K.). Stable Photoluminescence (PL) and time-resolved Photoluminescence (TRPL) spectra were measured by fluorescence spectrometer (Edinburgh, FLS1000, U.K.). PL quantum yield (PLQY) measurements were performed with HAMAMATSU PHOTONICS K.K (C13534-31). The *J-V* curve of the performance of f-PSCs was excited by the AM 1.5G 1-sun illumination solar simulator (Sol 3A Class AAA, Oriel, Newport, USA) of sunlight source, and the obtained physical model was converted and collected by

Keithley 2400. Before the test, standard silicon cell (91150V-KG3, Newport, USA) was used as a reference to calibrate the light intensity of the instrument according to ISO-17025 standard, and the effective area of the device was determined to be 0.049 cm^{-2} by a customized metal mask. Steady-state photocurrent and PCE output were tested by Keithley at the maximum power point (MPP) of *J-V* plots of the PSCs. The external quantum efficiency (EQE) spectra were obtained by the quantum efficiency measurement system (QE-R, Enlitech, Taiwan of China). Electrochemical impedance spectroscopy (EIS) was tested by electrochemical workstation (Zennium Zahner, Germany) in the condition of dark.

DFT calculation details

Density functional theory (DFT) calculations were performed using the Vienna Ab initio Simulation Package.[1,2] The projector augmented wave (PAW) method was employed to describe the ion-electron interactions, and the exchange-correlation energy was treated within the generalized gradient approximation (GGA) using the Perdew-Burke-Ernzerhof (PBE) functional.[3,4] To accurately describe the adsorption of the large organic molecule Me-4PACz on the oxide surface, the van der Waals (vdW) interactions were corrected using the DFT-D3 method with Becke-Johnson damping, as defined by Grimme.[5] The plane-wave cutoff energy was set to 400 eV. Electronic self-consistency was converged to 10-4 eV, and spin polarization was included to account for the magnetic properties of NiO. Geometry optimization was performed using the conjugate gradient algorithm until the forces on each relaxed atom were less than 0.04 eV/Å.

The NiO (111) surface was modeled using a slab geometry constructed from the conventional Fm-3m (225) unit cell. To minimize the interaction between periodic images, a vacuum layer of 25 Å was added along the z-direction. The surface supercell was expanded to a 5×5×1 configuration to accommodate the Me-4PACz [$C_{18}H_{22}NO_3P$] molecule. During the structural relaxation, the bottom two atomic layers of the NiO slab were fixed to their bulk positions, while the top two layers and the adsorbed molecule were

allowed to fully relax.

Two adsorption configurations involving dehydrogenation were investigated: (i) a monodentate mode where the dehydrogenated Me-4PACz fragment ($C_{18}H_{21}NO_3P$) bonds to one surface Ni atom, and (ii) a tridentate mode where the fragment ($C_{18}H_{20}NO_3P$) bonds to three Ni atoms centered around a surface oxygen vacancy. The binding energy (E_b) was calculated to evaluate the stability of the molecule-surface interaction, defined as:

$$E_b = E_{total} - E_{slab} - E_{mol}$$

where E_{total} is the total energy of the adsorption system, E_{slab} is the energy of the clean NiO surface (with an oxygen vacancy for the tridentate case), E_{mol} is the energy of the isolated intact Me-4PACz molecule. According to this definition, a more negative value indicates a stronger binding interaction.

Supplementary Note 1: Residual stress analysis by GIXRD.

For the GIXRD measurement, the XRD peak at 31.6° of the perovskite (210) plane is selected as the stress-free 2θ degrees reference plane because of its diversity, which can provide more reliable structural symmetry information. In this process, 2θ degrees remains constant, and by adjusting the tilt angle of the instrument, the penetration depth of the X-ray can be ensured. In the experiment, the tilt angle (ψ) is set to 5°, 15°, 25°, 35°, and 45°, respectively. Based on Bragg's Law and the generalized Hooke's Law, the relationship between 2θ-$\sin^2\psi$ can be expressed by equation:

$$\sigma = -\frac{E}{(1+\nu)}\frac{\pi}{180^\circ}cot\theta_0\frac{\partial(2\theta_0)}{\partial(Sin_\psi)^2}$$

where E is the modulus of the perovskite (E=10 GPa), ν is the Poisson's ratio of the perovskite (ν =0.3), and θ_0 is half of the scattering angle 2θ, corresponding to the given diffraction peak of the stress-free perovskite ($2\theta_0$ = 31.6°).[6,7] The residual stress in perovskite films can be calculated by fitting the function of 2θ-$\sin^2\psi$. The slope of the fitted line reflects the magnitude of the residual strain. A negative slope indicates that the thin film is under tensile stress, whereas a positive slope suggests that the thin film is under compressive stress.

Supplementary Note 2: Fill factor (FF) loss analysis.

According to the S-Q limit theory, non-radiative recombination and charge transport losses are responsible for the measured FF falling below the theoretical value.[8] The lower the non-radiative recombination loss of the device, the higher its maximum FF (FF_{max}) value. The FF_{max} can be calculated using the following equation:

$$FF_{max} = \frac{v_{OC} - ln(v_{OC} + 0.72)}{v_{OC} + 1}$$

The v_{OC} can be obtained by the following equation:

$$v_{OC} = \frac{V_{OC}}{nK_BT/q}$$

where n is the ideality factor extracted from the slope of the V_{OC}-light dependence curve (Fig. S33). K_B is Boltzmann constant, and T is the temperature (300 K).

Substituting the n value into the aforementioned equation yields the FF_{max} (87.57%) and measured FF (87.04%) for the target device, both higher than those of the control group (84.50% and 83.64%), with corresponding *FF* losses of 0.53% and 0.86%, respectively.

Figures and Tables

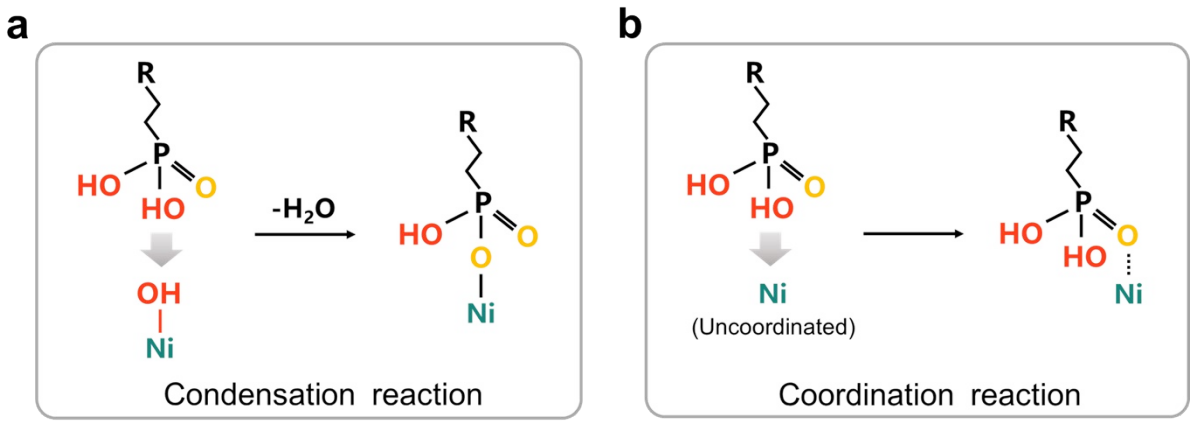

Fig. S1 Schematic of the chemical reactions between SAM and the NiO_x. (a) Condensation reaction between P-OH (on SAM) and surface OH (on NiO_x). (b) Coordination of the SAM to undercoordinated Ni ions (on NiO_x).

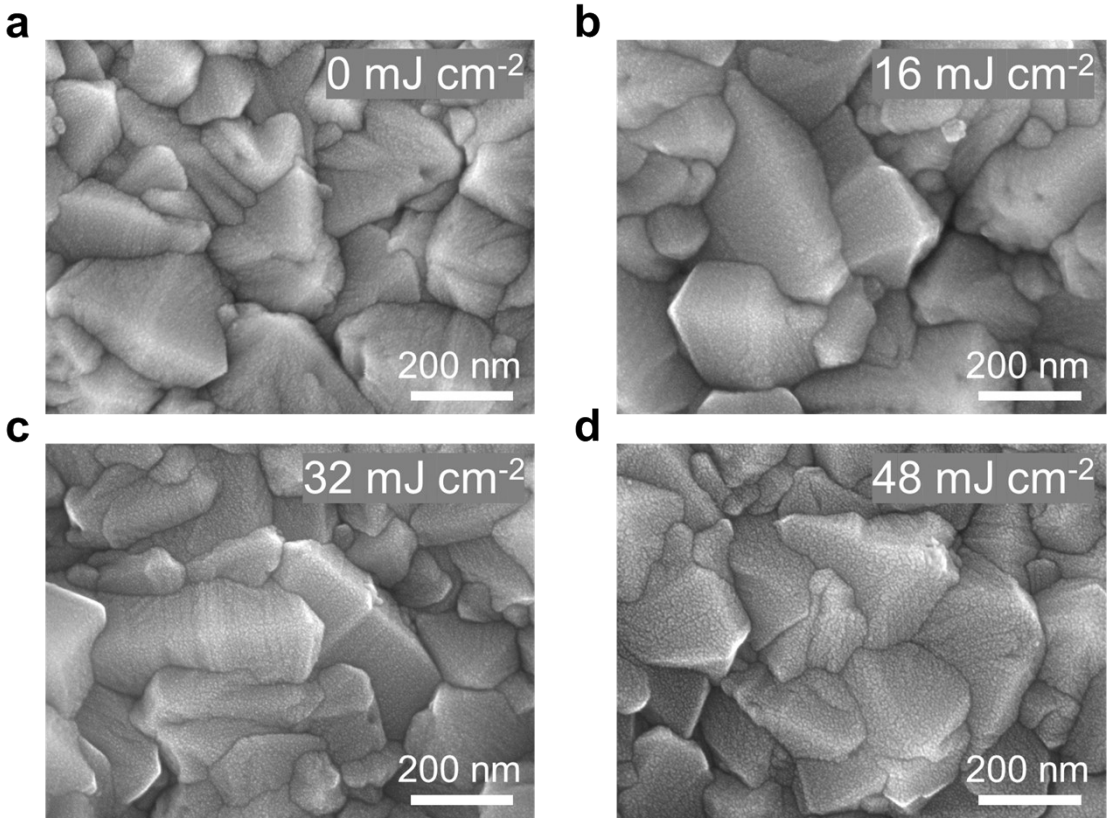

Fig. S2 SEM images of sputtered NiO_x films under laser intensities of (a) 0 mJ cm^{-2}, (b) 16 mJ cm^{-2}, (c) 32 mJ cm^{-2}, and (d) 48 mJ cm^{-2}, respectively.

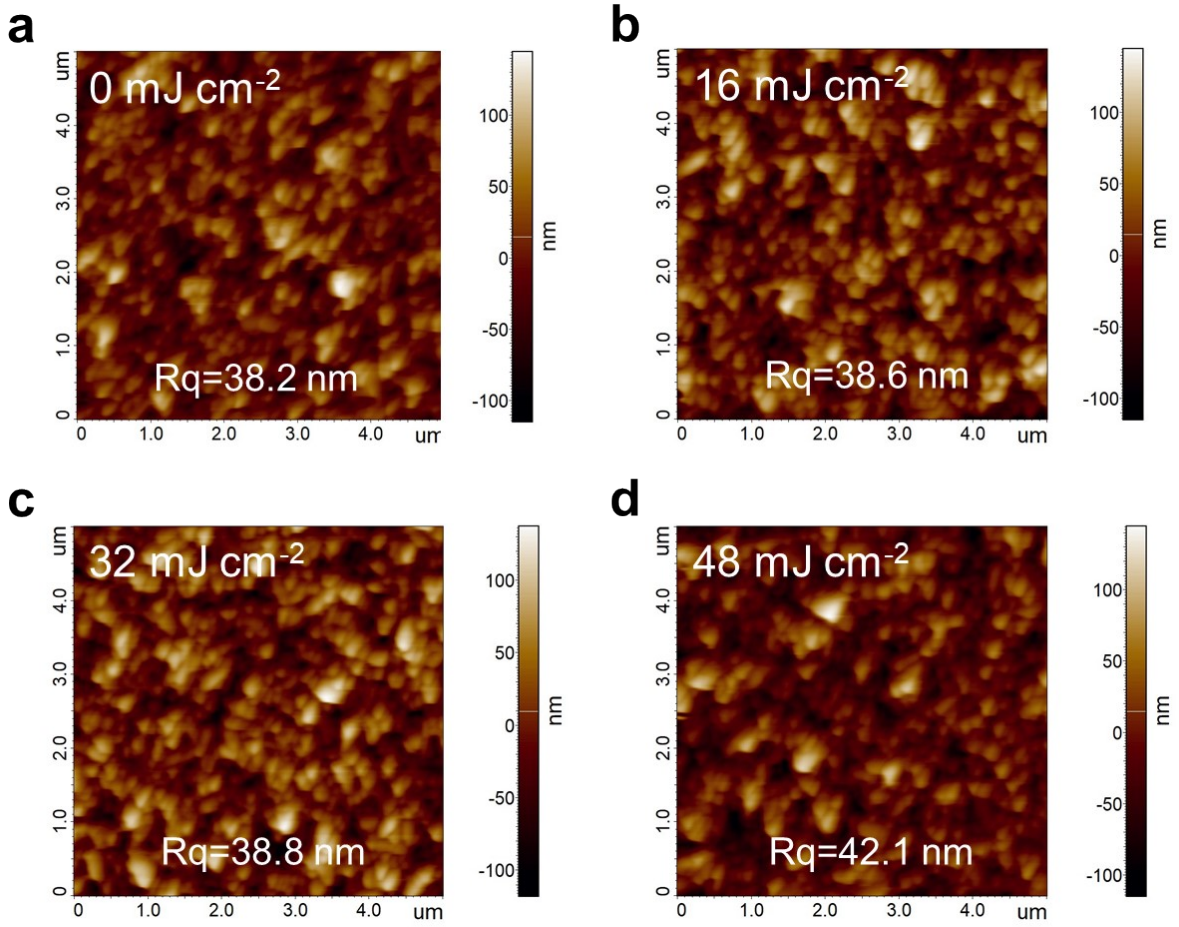

Fig. S3 AFM images of sputtered NiO_x films under laser intensities of (a) 0 mJ cm^{-2}, (b) 16 mJ cm^{-2}, (c) 32 mJ cm^{-2}, and (d) 48 mJ cm^{-2}, respectively.

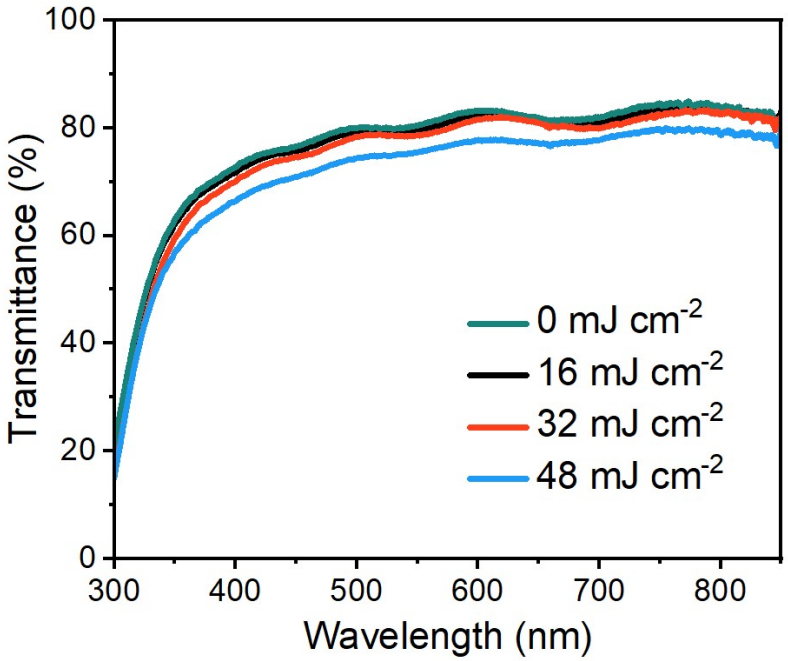

Fig. S4 Optical transmission spectra of sputtered NiO_x films under laser intensities of (a) 0 mJ cm^{-2}, (b) 16 mJ cm^{-2}, (c) 32 mJ cm^{-2}, and (d) 48 mJ cm^{-2}, respectively.

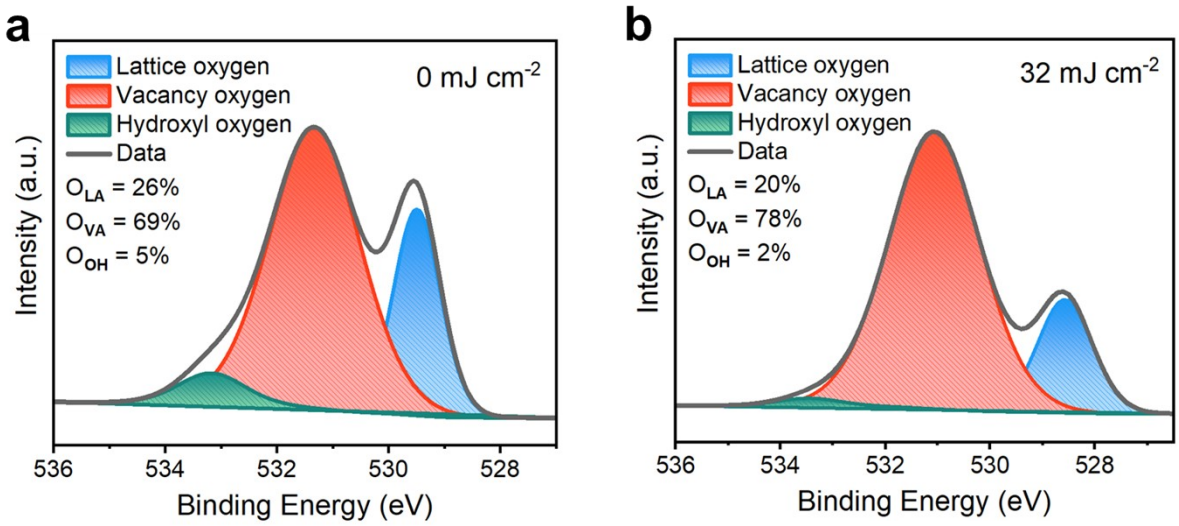

Fig. S5 High-resolution O 1s XPS spectra of the NiO_x films under laser irradiation at intensities of (a) 0 mJ cm^{-2} and (b) 32 mJ cm^{-2}, respectively.

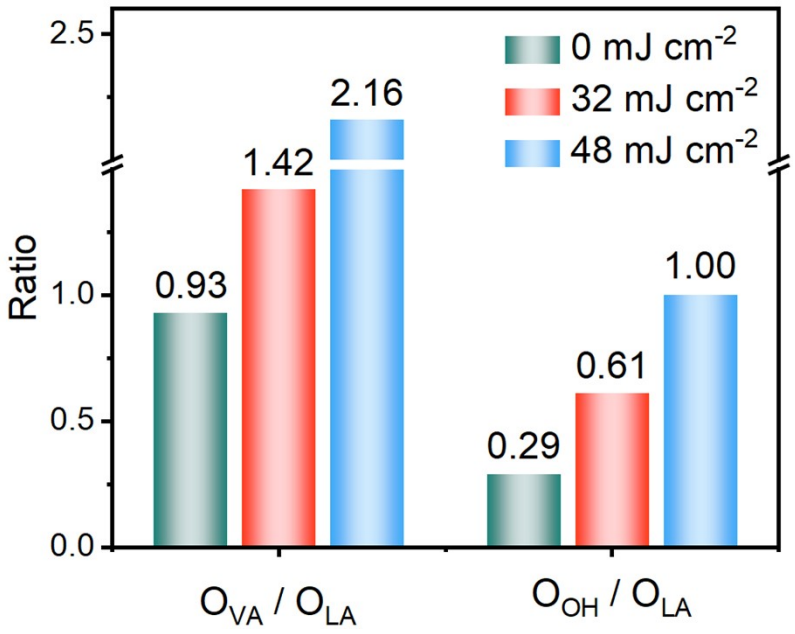

Fig. S6 Ratios of vacancy oxygen (O_{VA}) to lattice oxygen (O_{LA}), and hydroxyl oxygen (O_{OH}) to O_{LA}.

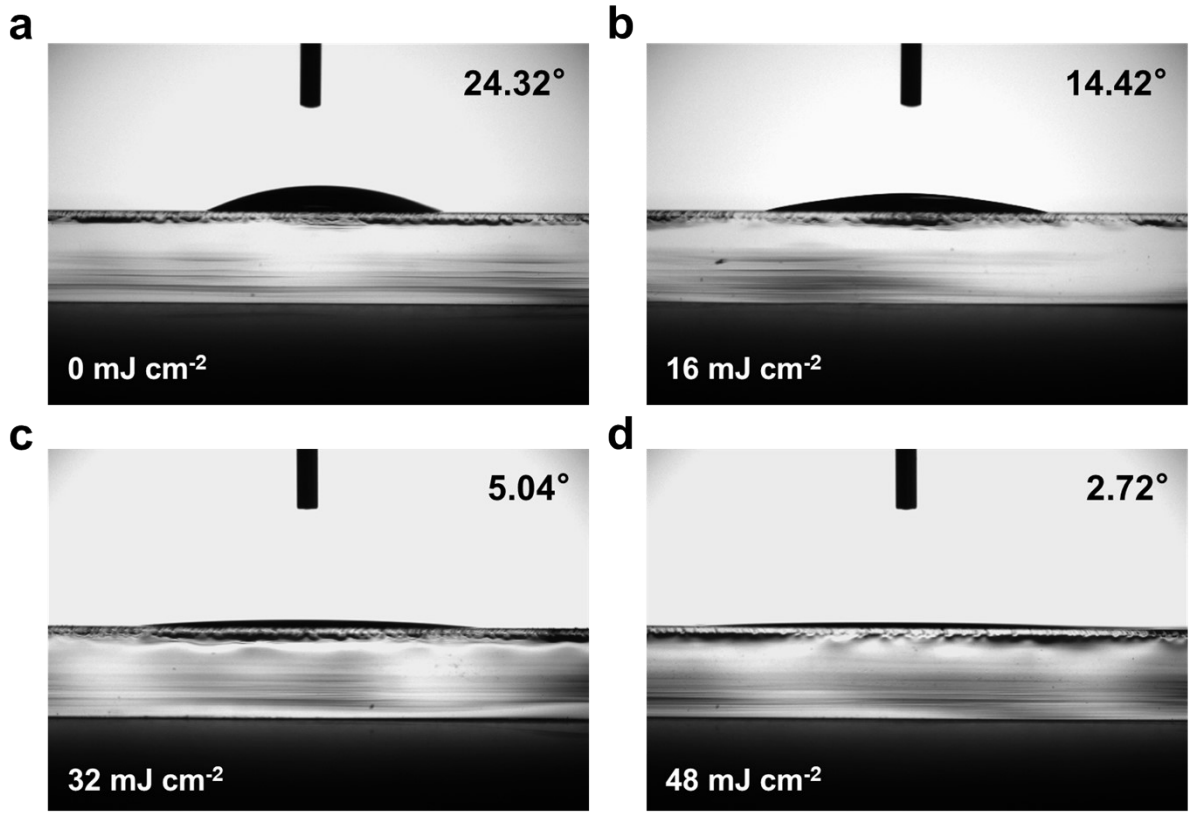

Fig. S7 Water contact angle of NiO_x films under laser intensities of (a) 0 mJ cm^{-2}, (b) 16 mJ cm^{-2}, (c) 32 mJ cm^{-2}, and (d) 48 mJ cm^{-2}, respectively.

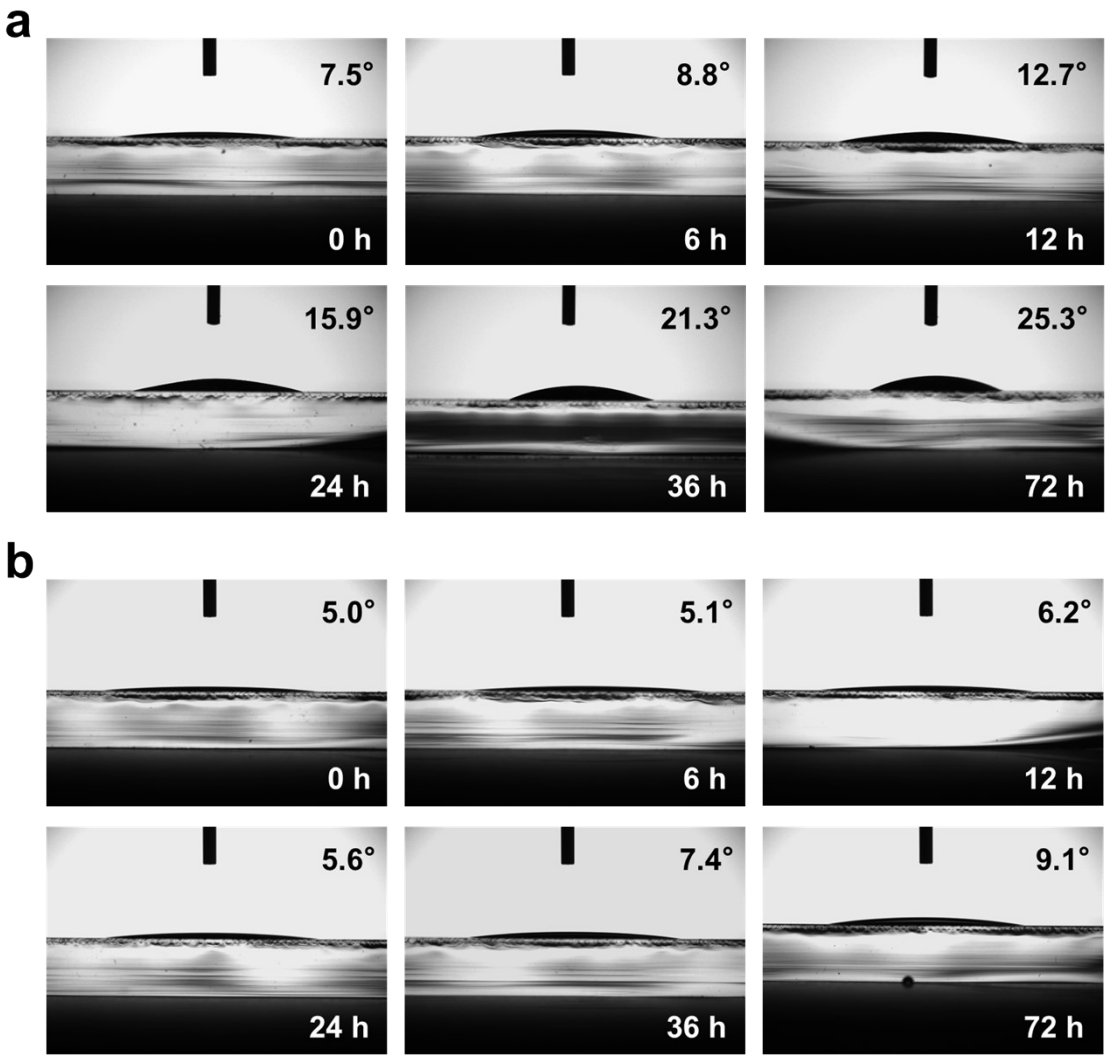

Fig. S8 Changes in water contact angles on (a) plasma-treated control and (b) target NiO_x films over different storage times.

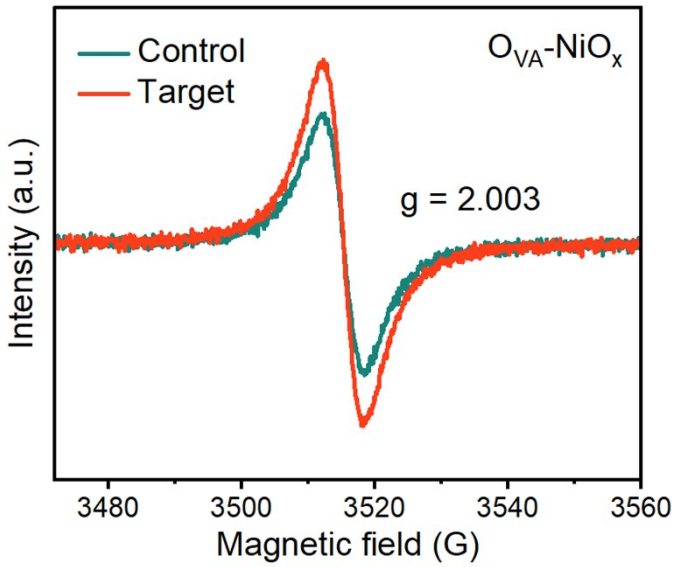

Fig. S9 Electron paramagnetic resonance (EPR) spectra for the control and target NiO_x films.

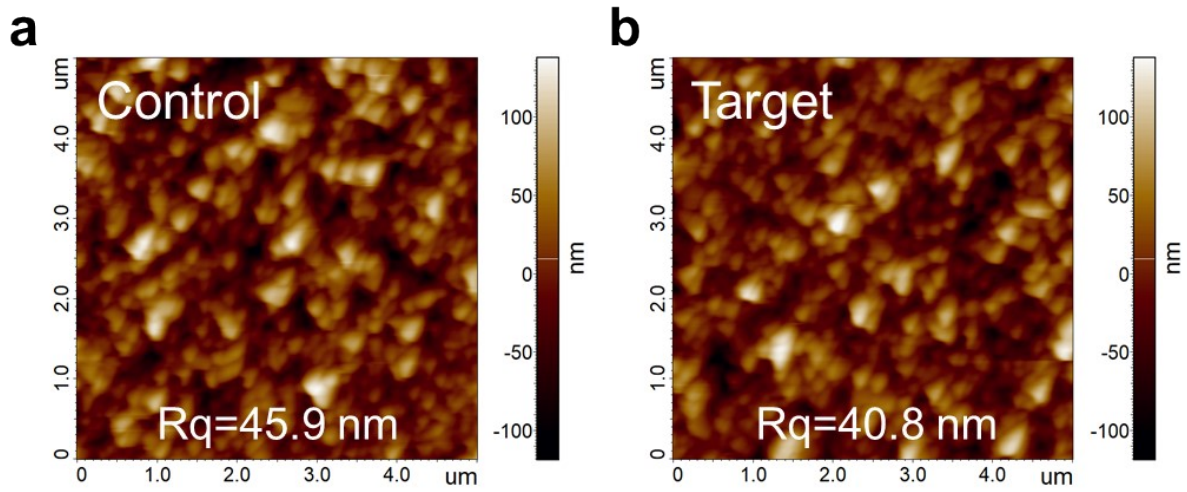

Fig. S10 AFM morphology images of (a) control NiO_x/SAM and (b) target NiO_x/SAM, respectively.

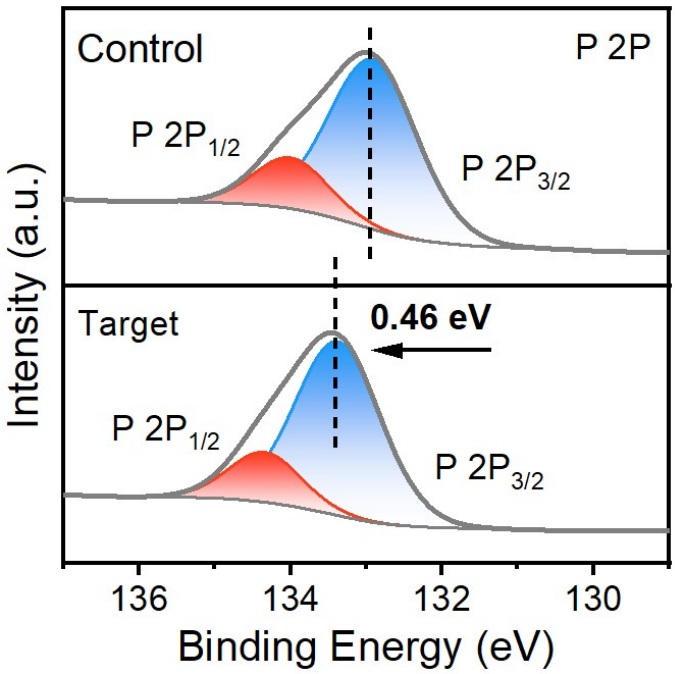

Fig. S11 XPS core level spectra of P 2p for control and target NiO_x after SAM anchoring.

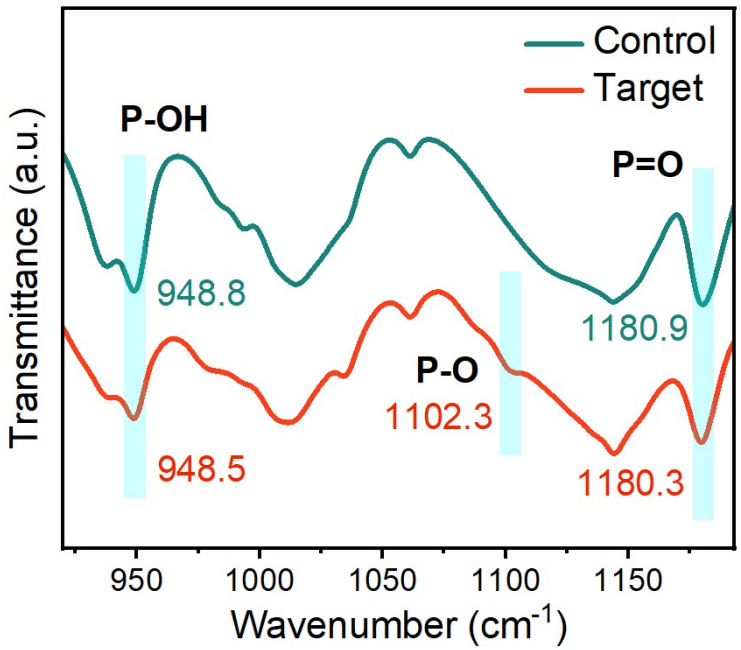

Fig. S12 FTIR spectra of SAMs assembled on different NiO_x.

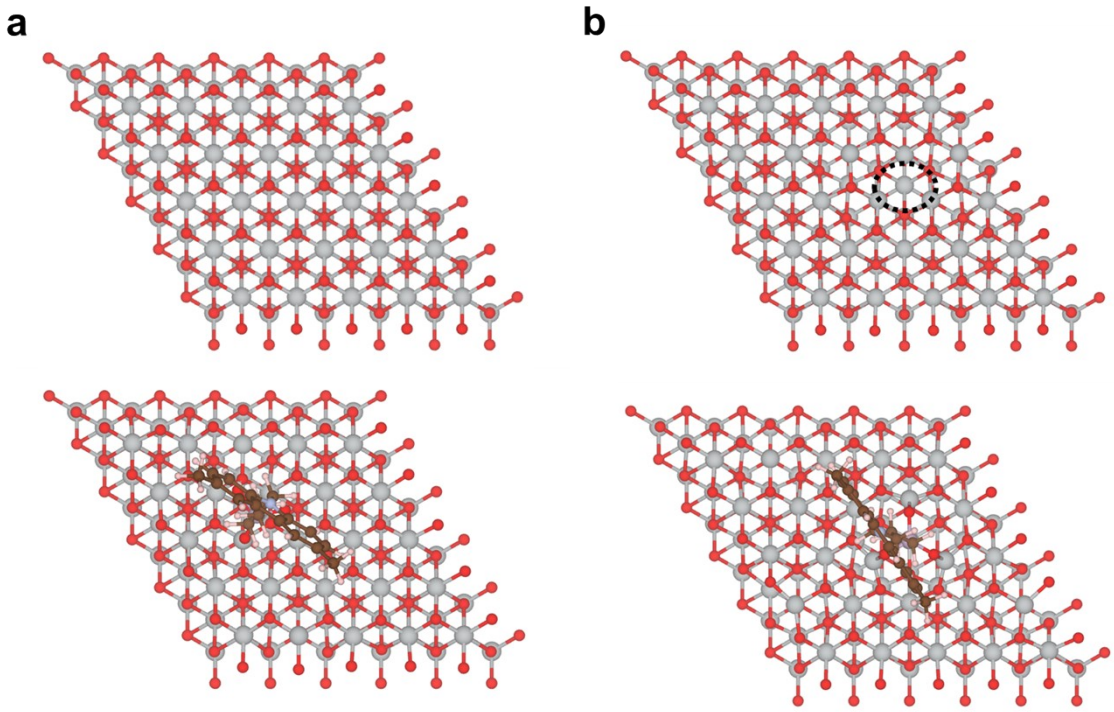

Fig. S13. (a) Pristine and (b) oxygen-deficient NiO, and the corresponding NiO/SAM models for DFT calculation of binding energy.

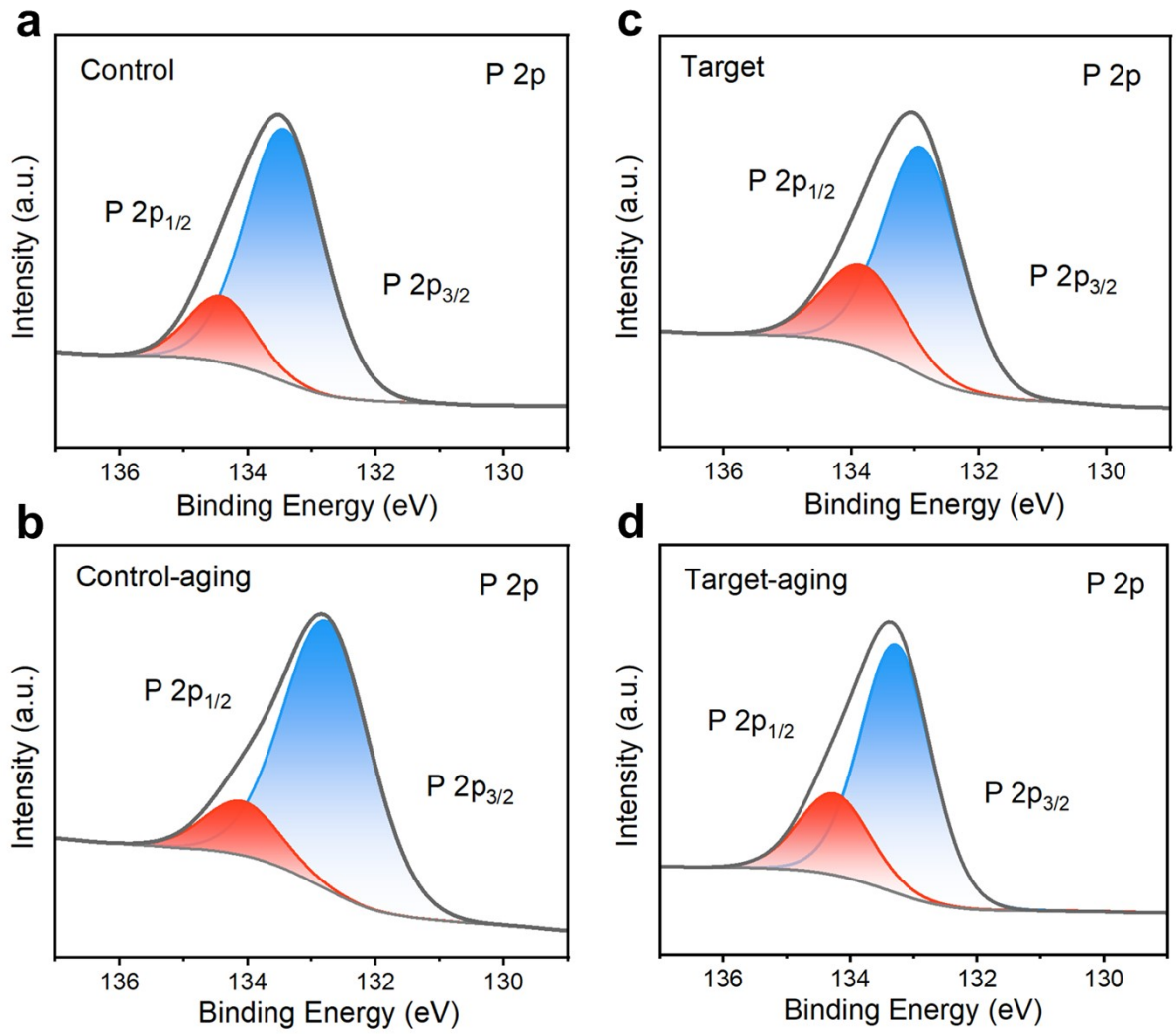

Fig. S14. P 2p XPS spectra of the control NiO_x/SAM substrates (a) before and (b) after thermal aging, and of the target NiO_x/SAM substrates (c) before and (d) after the same treatment.

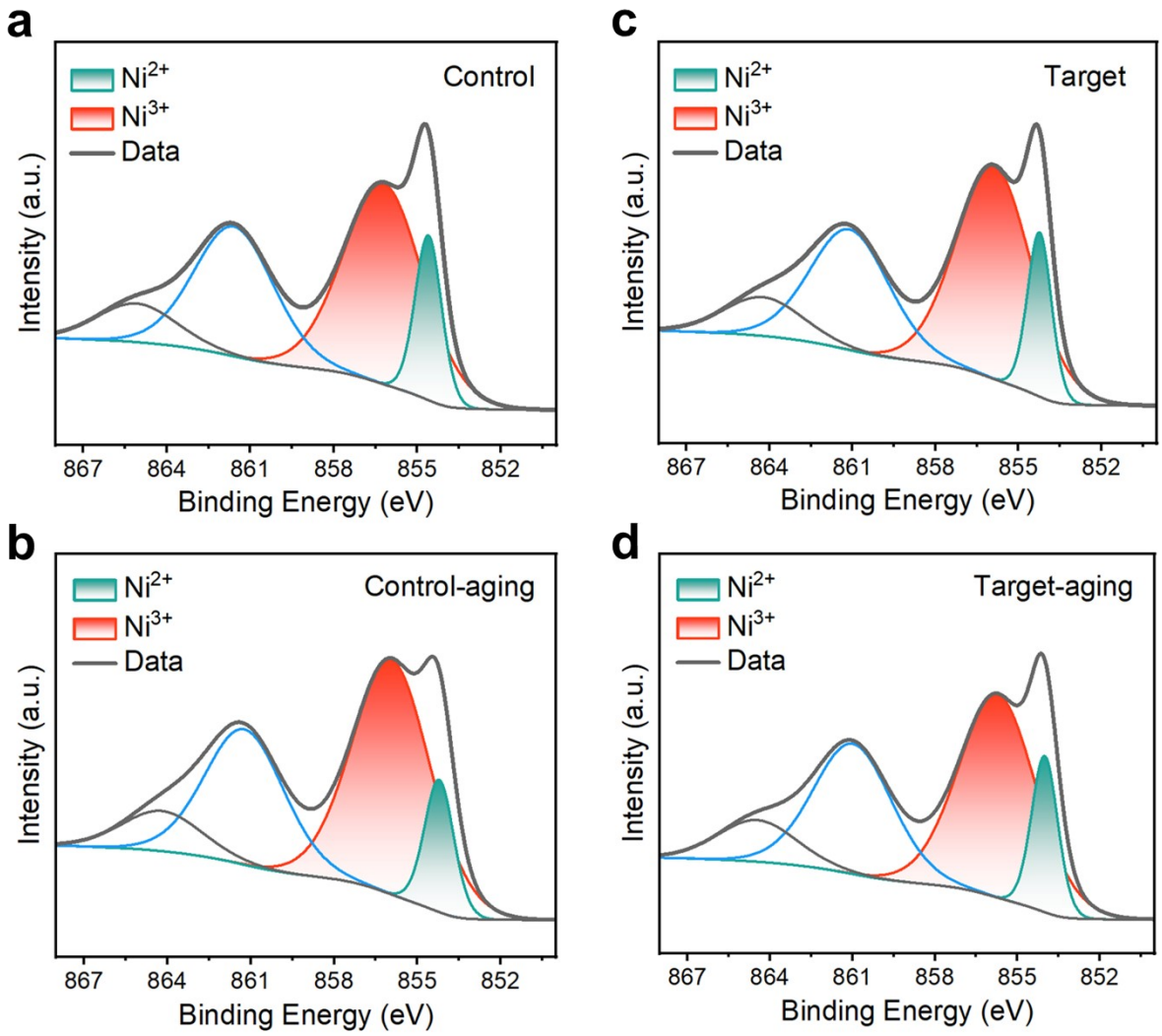

Fig. S15 Ni 2p XPS spectra of the control NiO_x/SAMs substrates (a) before and (b) after thermal aging, and of the target NiO_x/SAMs substrates (c) before and (d) after the same treatment.

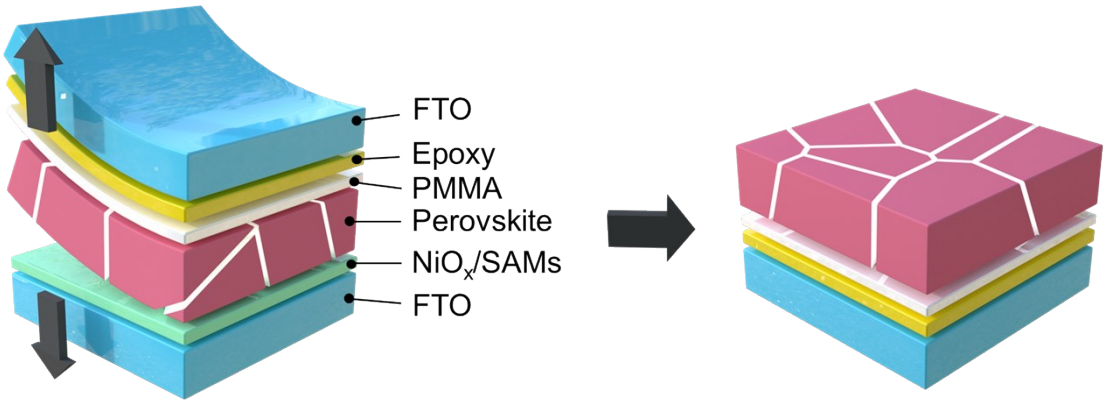

Fig. S16 Schematic of the preparation of the buried perovskite surface.

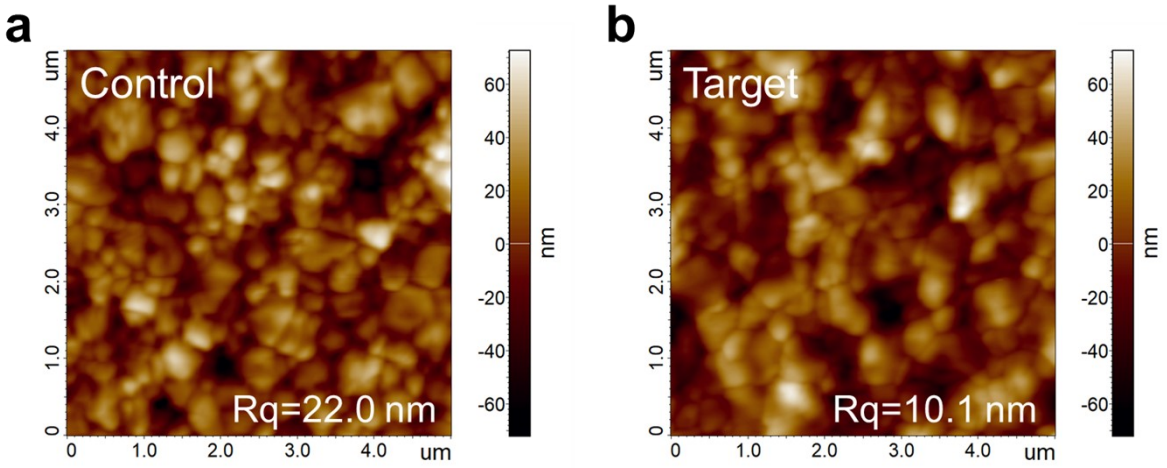

Fig. S17 AFM images of the buried surface of perovskite films deposited on (a) control and (b) target NiO_x/SAMs, respectively.

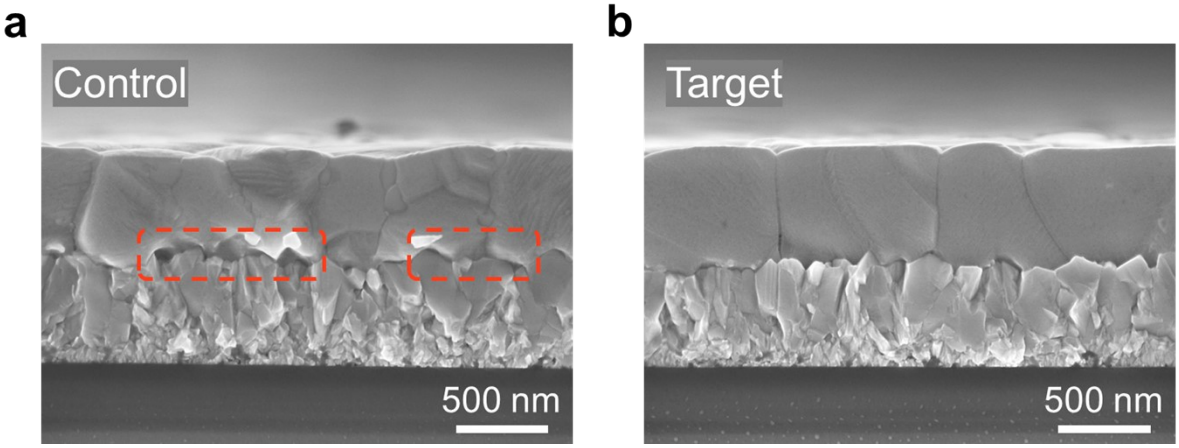

Fig. S18 Cross-section SEM images of perovskite film on (a) control and (b) target NiO_x/SAMs, respectively.

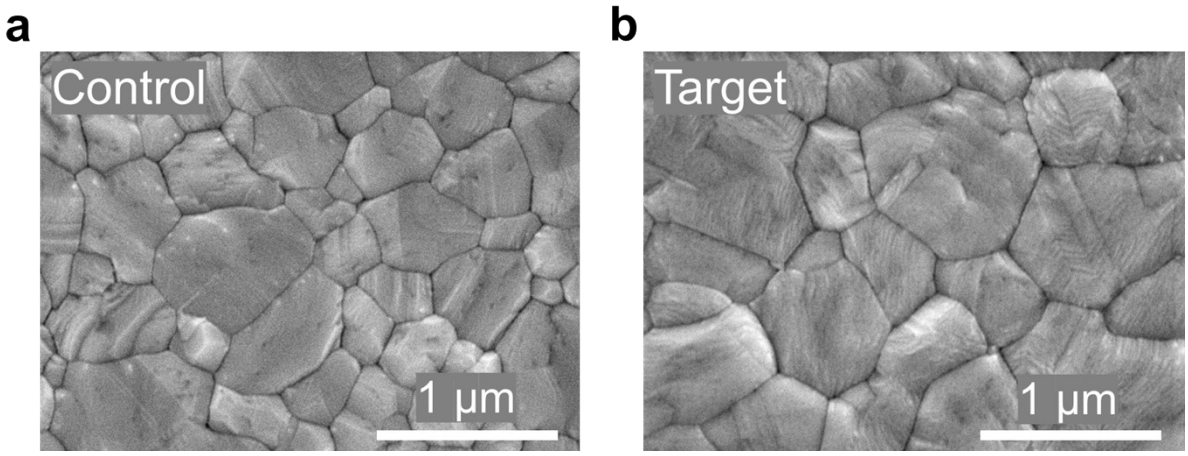

Fig. S19 SEM images of the top surface of perovskite films deposited on (a) control and (b) target NiO_x/SAMs, respectively.

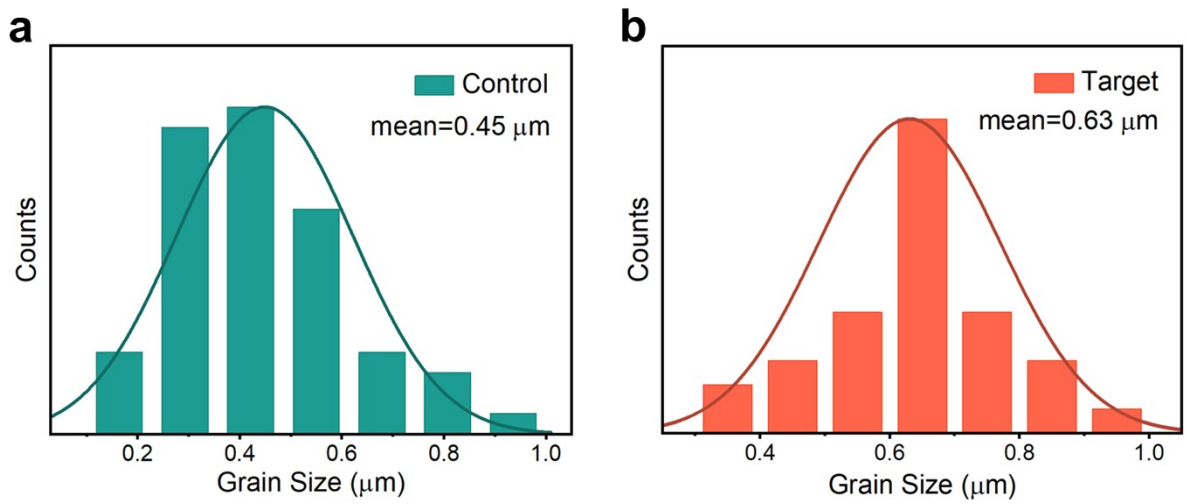

Fig. S20 Size distribution of the top surface of perovskite films deposited on (a) control and (b) target NiO_x/SAMs, respectively.

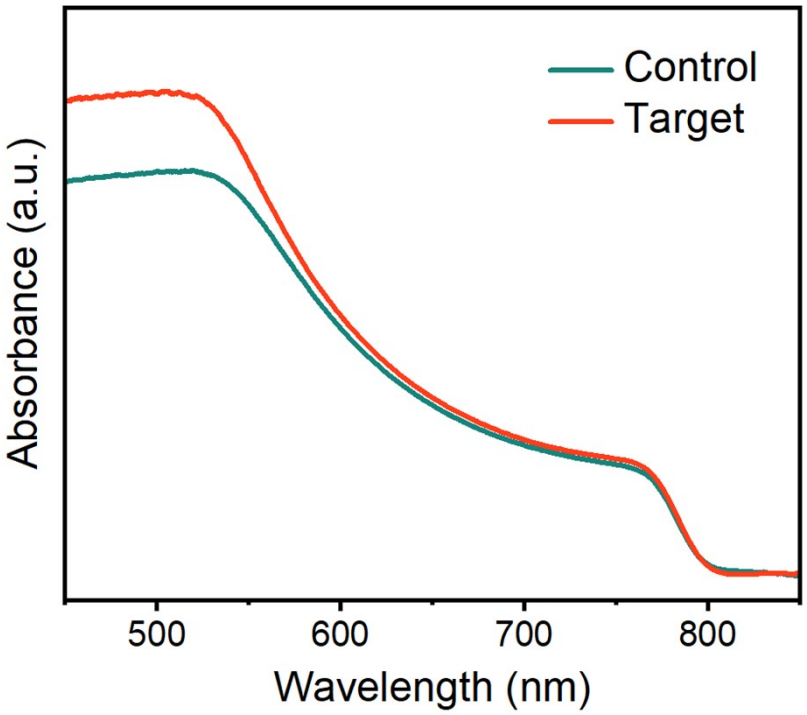

Fig. S21 UV-vis absorption spectra of perovskite films deposited on different NiO_x/SAMs.

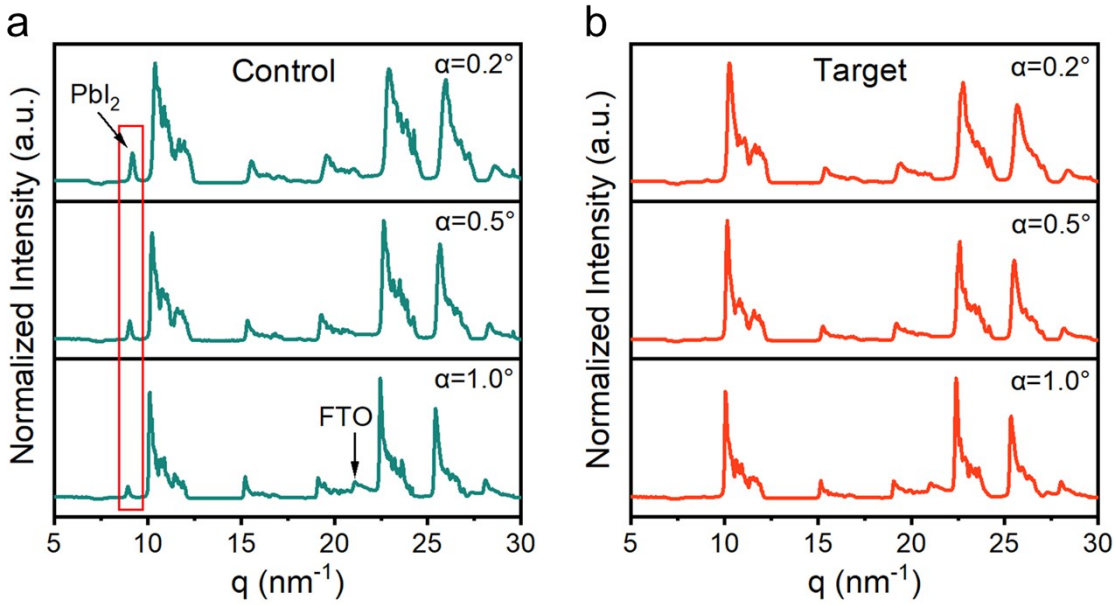

Fig. S22 1D integral analysis for (a) control and (b) target GIWAXS patterns.

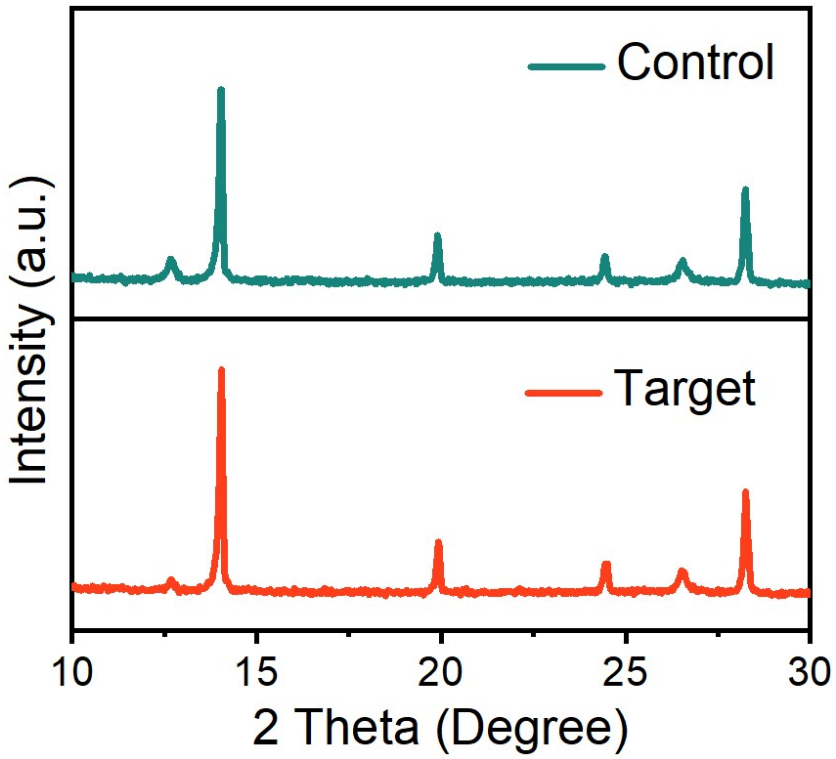

Fig. S23 XRD patterns of the buried surface of perovskite films deposited on different NiO_x/SAMs.

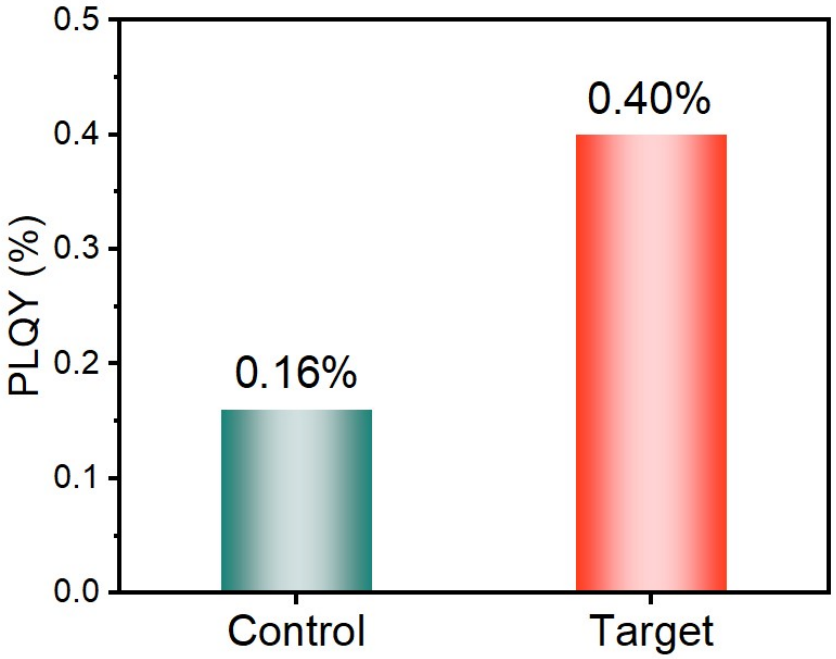

Fig. S24 The PLQY of the exposed buried perovskite surface deposited on different NiO_x/SAMs.

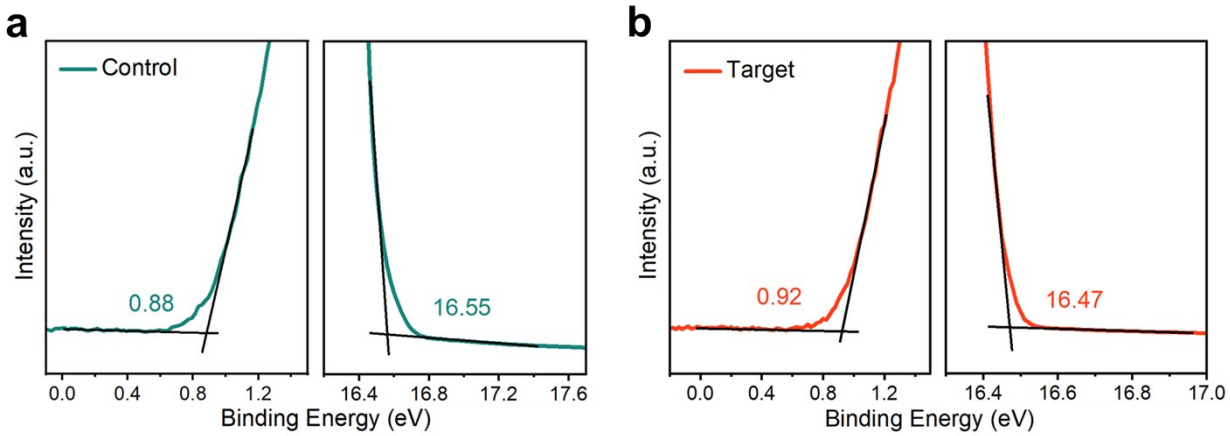

Fig. S25 UPS spectra of (a) control and (b) target NiO_x/SAMs, respectively.

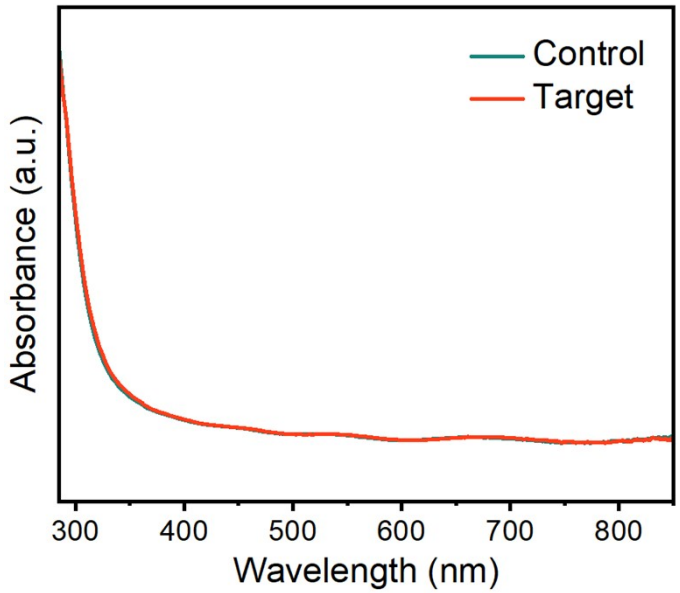

Fig. S26 UV-vis absorption spectra of different NiO_x/SAMs.

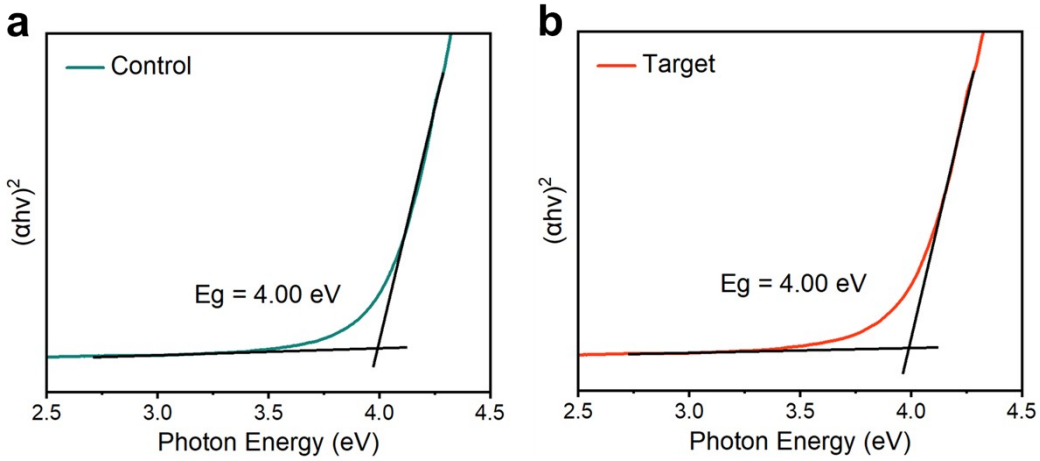

Fig. S27 Tauc plots of (a) control and (b) target NiO_x/SAMs, respectively.

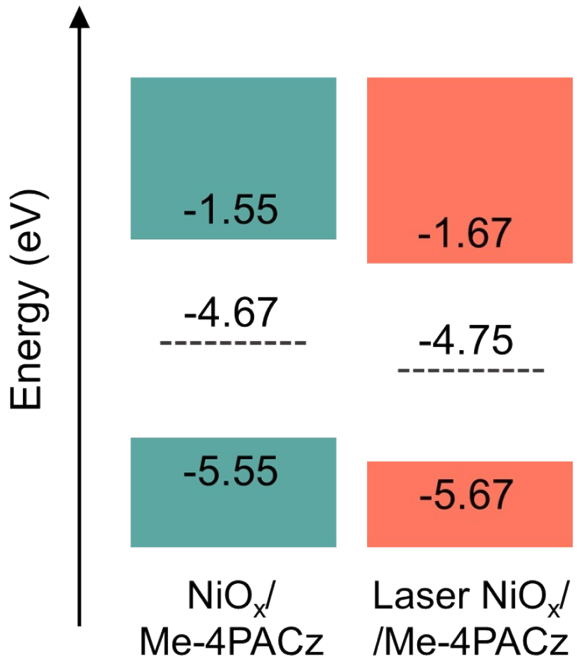

Fig. S28 Schematic diagram of energy levels of VBM and conduction band minimum (CBM) derived from UPS spectra of the different NiO_x/SAMs.

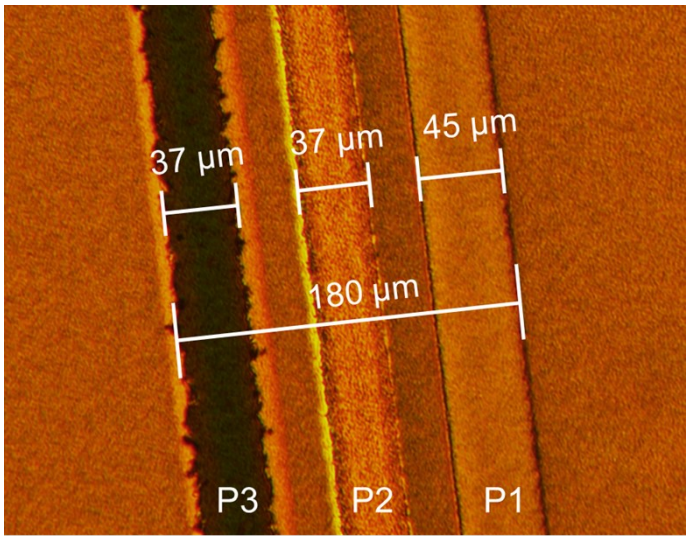

Fig. S29 Morphology of laser etching lines and widths of P1, P2, and P3 in large-area PSMs.

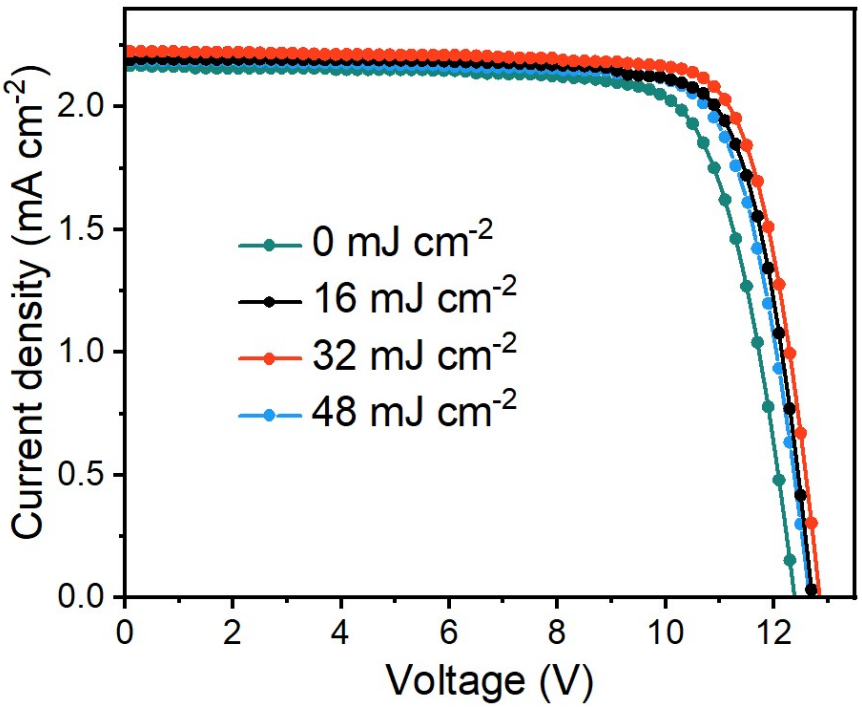

Fig. S30 *J-V* curves of PSMs with different laser intensities.

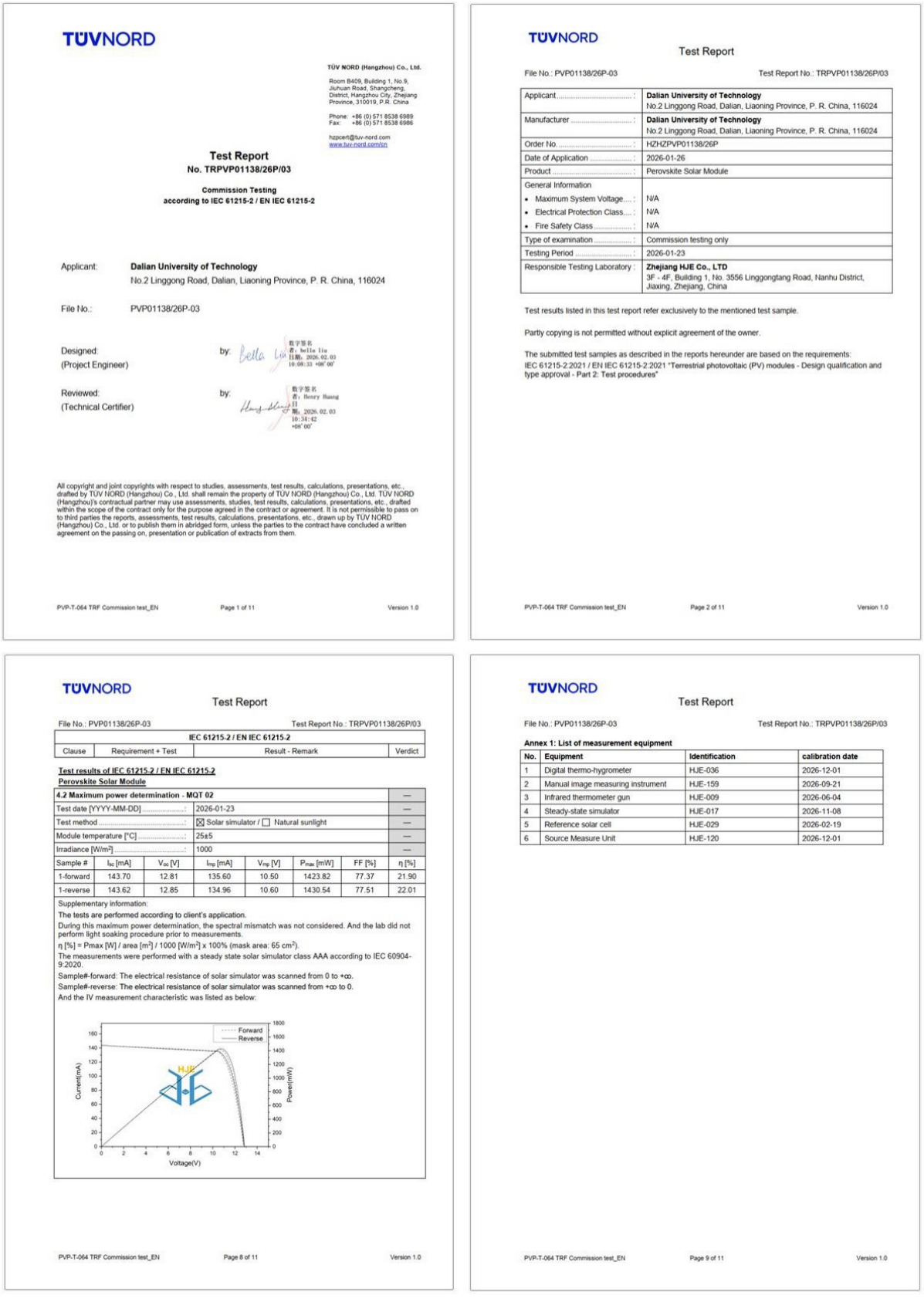

TÜVNORD

TÜV NORD (Hangzhou) Co., Ltd.
Room B409, Building 1, No.9, Jiuhuan Road, Shangcheng, District, Hangzhou City, Zhejiang Province, 310019, P.R. China
Phone: +86 (0) 571 8538 6989
Fax: +86 (0) 571 8538 6986
hzpcert@tuv-nord.com
www.tuv-nord.com/cn

Test Report
No. TRPVP01138/26P/03

Commission Testing
according to IEC 61215-2 / EN IEC 61215-2

Applicant: **Dalian University of Technology**
No.2 Linggong Road, Dalian, Liaoning Province, P. R. China, 116024

File No.: PVP01138/26P-03

Designed: by: 数字签名 者：bella liu 日期：2026.02.03 10:08:33 +08'00'
(Project Engineer)

Reviewed: by: 数字签名 者：Henry Huang 日 期：2026.02.03 10:34:42 +08'00'
(Technical Certifier)

TÜVNORD

Test Report

File No.: PVP01138/26P-03 Test Report No.: TRPVP01138/26P/03

Applicant:	**Dalian University of Technology** No.2 Linggong Road, Dalian, Liaoning Province, P. R. China, 116024
Manufacturer:	**Dalian University of Technology** No.2 Linggong Road, Dalian, Liaoning Province, P. R. China, 116024
Order No.:	HZHZPVP01138/26P
Date of Application:	2026-01-26
Product:	Perovskite Solar Module
General Information	
• Maximum System Voltage:	N/A
• Electrical Protection Class:	N/A
• Fire Safety Class:	N/A
Type of examination:	Commission testing only
Testing Period:	2026-01-23
Responsible Testing Laboratory:	**Zhejiang HJE Co., LTD** 3F - 4F, Building 1, No. 3556 Linggongtang Road, Nanhu District, Jiaxing, Zhejiang, China

Test results listed in this test report refer exclusively to the mentioned test sample.

Partly copying is not permitted without explicit agreement of the owner.

The submitted test samples as described in the reports hereunder are based on the requirements:
IEC 61215-2:2021 / EN IEC 61215-2:2021 "Terrestrial photovoltaic (PV) modules - Design qualification and type approval - Part 2: Test procedures"

TÜVNORD

Test Report

File No.: PVP01138/26P-03 Test Report No.: TRPVP01138/26P/03

IEC 61215-2 / EN IEC 61215-2			
Clause	Requirement + Test	Result - Remark	Verdict

Test results of IEC 61215-2 / EN IEC 61215-2
Perovskite Solar Module

4.2 Maximum power determination - MQT 02		—
Test date [YYYY-MM-DD]	2026-01-23	—
Test method	☒ Solar simulator / ☐ Natural sunlight	—
Module temperature [°C]	25±5	—
Irradiance [W/m²]	1000	—

Sample #	I_{sc} [mA]	V_{oc} [V]	I_{mp} [mA]	V_{mp} [V]	P_{max} [mW]	FF [%]	η [%]
1-forward	143.70	12.81	135.60	10.50	1423.82	77.37	21.90
1-reverse	143.62	12.85	134.96	10.60	1430.54	77.51	22.01

Supplementary information:
The tests are performed according to client's application.
During this maximum power determination, the spectral mismatch was not considered. And the lab did not perform light soaking procedure prior to measurements.
η [%] = Pmax [W] / area [m²] / 1000 [W/m²] x 100% (mask area: 65 cm²).
The measurements were performed with a steady state solar simulator class AAA according to IEC 60904-9:2020.
Sample#-forward: The electrical resistance of solar simulator was scanned from 0 to +∞.
Sample#-reverse: The electrical resistance of solar simulator was scanned from +∞ to 0.
And the IV measurement characteristic was listed as below:

TÜVNORD

Test Report

File No.: PVP01138/26P-03 Test Report No.: TRPVP01138/26P/03

Annex 1: List of measurement equipment

No.	Equipment	Identification	calibration date
1	Digital thermo-hygrometer	HJE-036	2026-12-01
2	Manual image measuring instrument	HJE-159	2026-09-21
3	Infrared thermometer gun	HJE-009	2026-06-04
4	Steady-state simulator	HJE-017	2026-11-08
5	Reference solar cell	HJE-029	2026-02-19
6	Source Measure Unit	HJE-120	2026-12-01

Fig. S31 The certification report of the PSM with an aperture area of 65 cm^2, issued by the TÜV NORD (Hangzhou) Co., Ltd.. The certified PCE is 22.01% with a V_{OC} of 12.85 V, a I_{SC} of 143.62 mA and an FF of 77.51%.

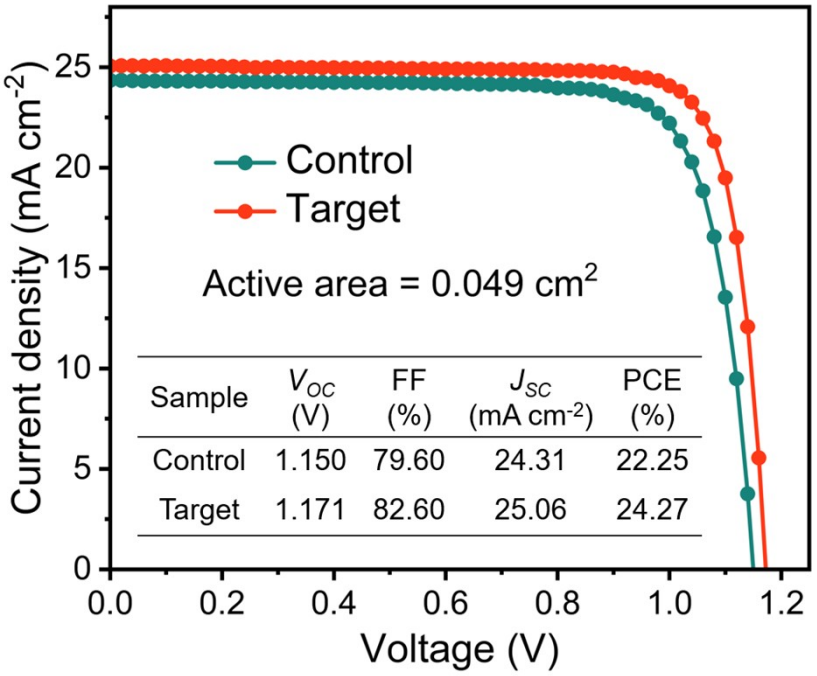

Fig. S32 *J-V* curves of PSCs with an active area of 0.049 cm^2.

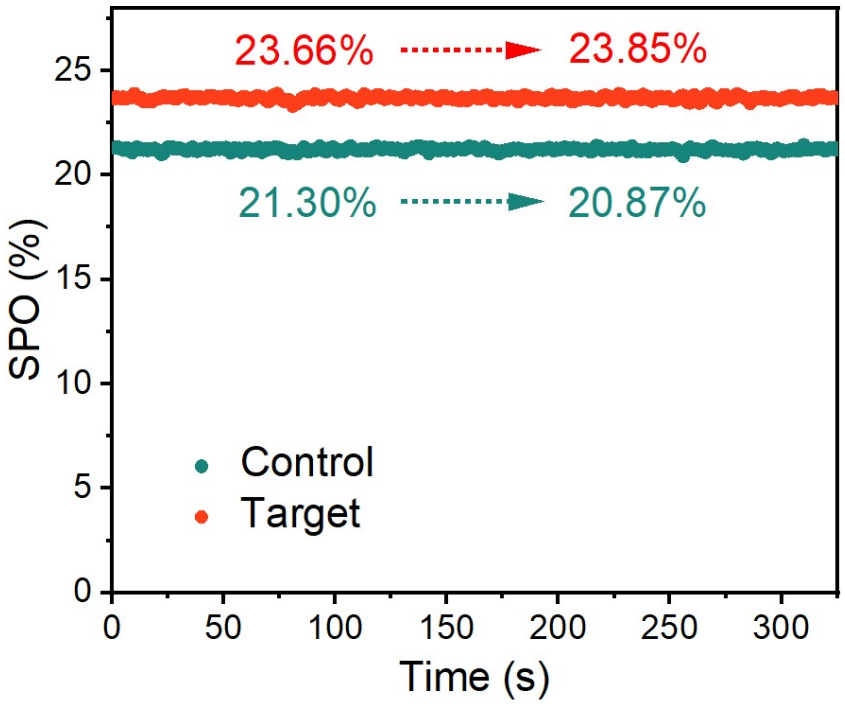

Fig. S33 Small area devices' steady power output (SPO) for 350 s.

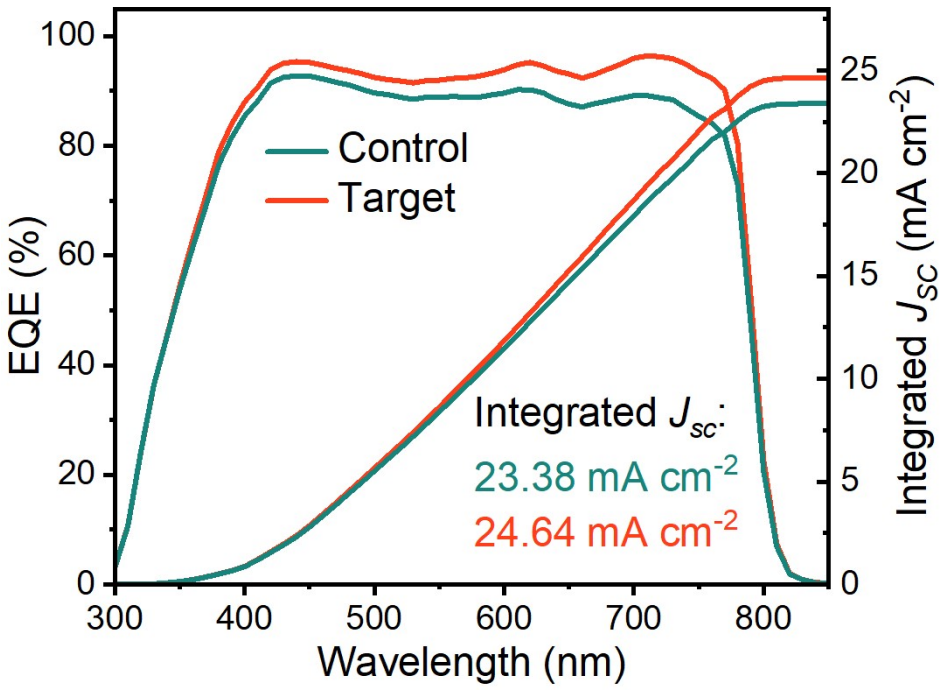

Fig. S34 EQE and corresponding integrated J_{SC} of small area PSCs.

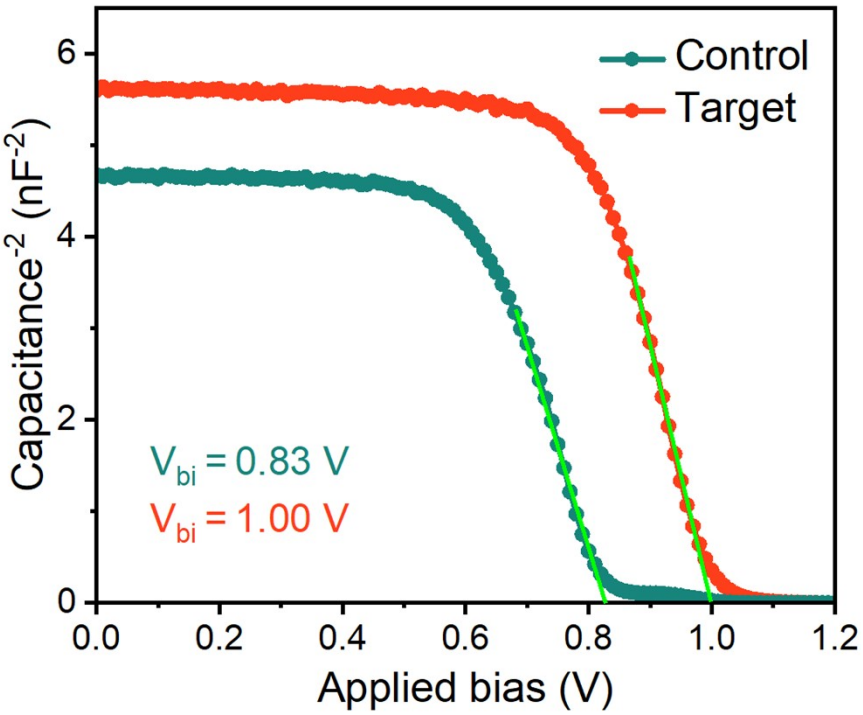

Fig. S35 Mott-Schottky plots of small area PSCs.

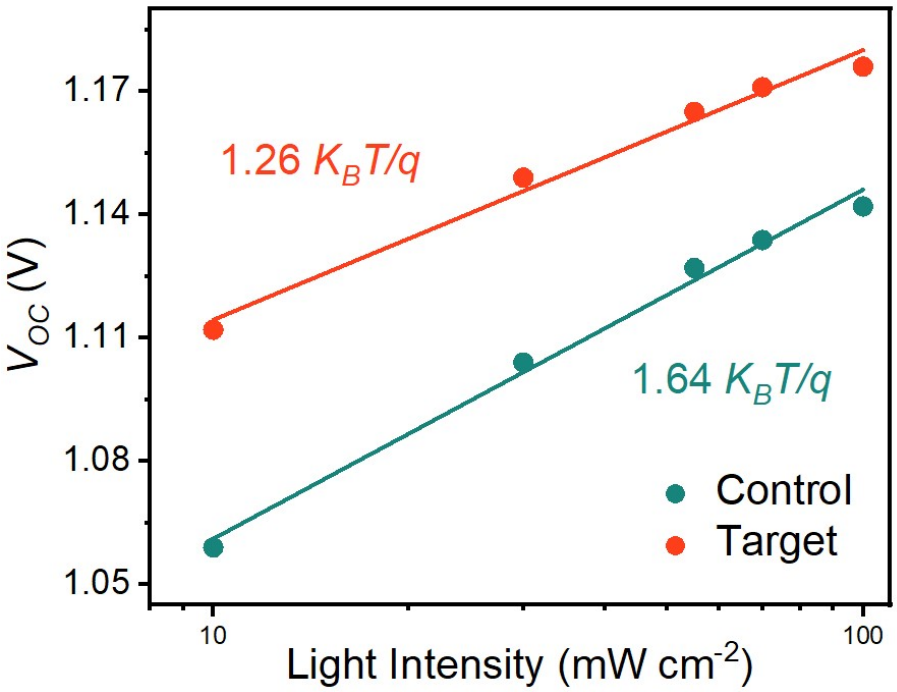

Fig. S36 V_{OC}-light intensity curves of small area PSCs.

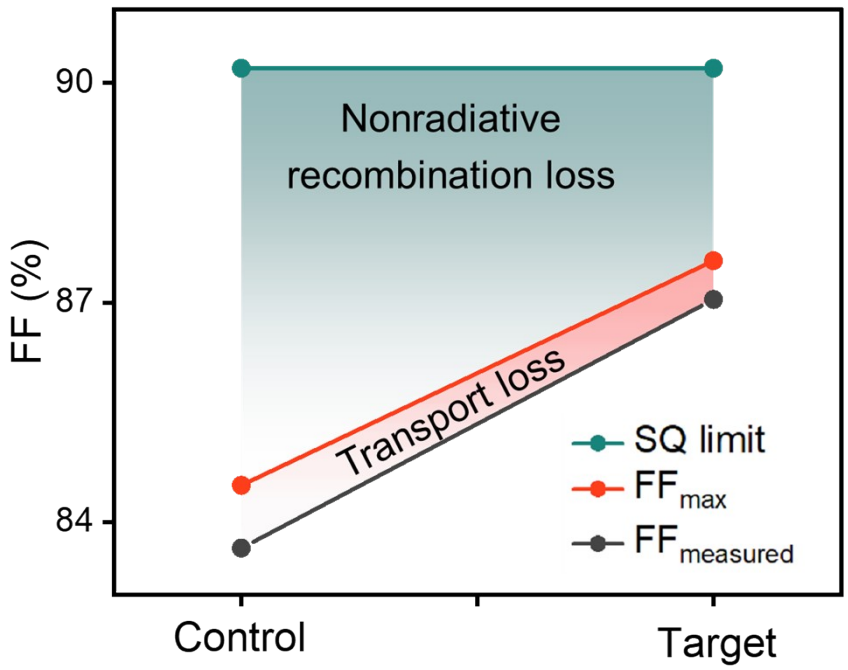

Fig. S37 FF loss analysis of small area PSCs.

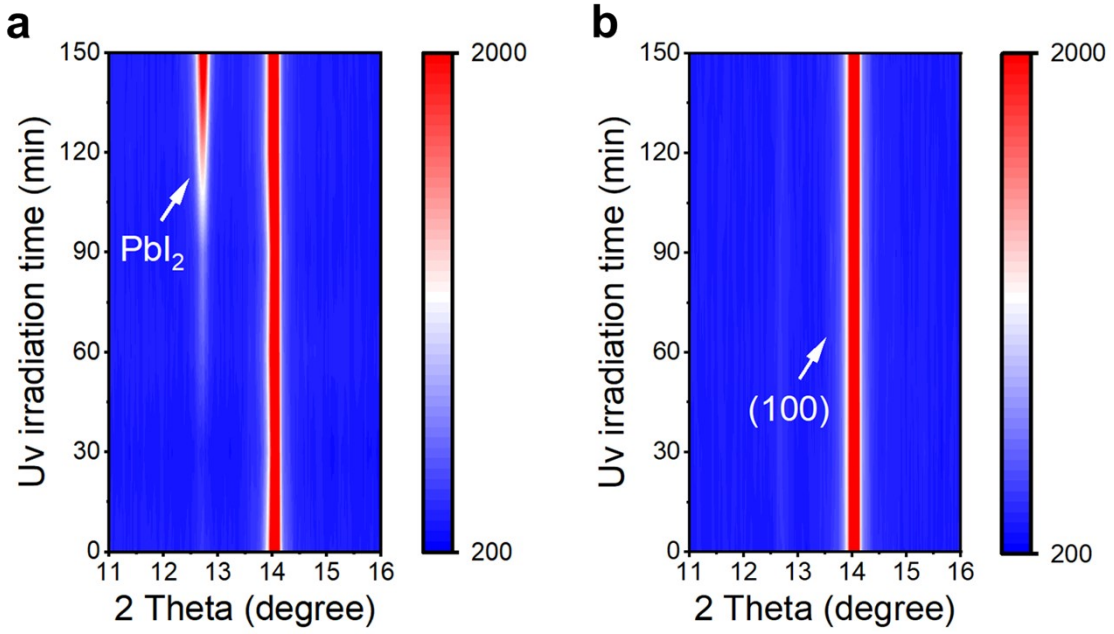

Fig. S38 In-situ XRD monitored the crystallization evolution of large area perovskite films on (a) control and (b) target NiOx/SAMs under continuous UV aging.

Table S1. Detailed data of DFT for binding energy of SAM on pristine NiO and NiO with O_{VA}.

Sample	***E*_total /eV**	***E*_slab /eV**	***E*_mol /eV**	***E*_binding /eV**
NiO	-1132.20	-853.25	-275.89	-3.06
NiO-O_{VA}	-1123.51	-846.78	-270.14	-6.59

Table S2. TRPL parameters of perovskite films under excitation from FTO-side incident light.

Sample	**A_1**	**τ_1 [ns]**	**A_2**	**τ_2 [ns]**	**τ_{ave} [ns]**
Control	0.10	23.14	0.81	354.74	352.09
Target	0.22	78.81	0.67	1075.25	1064.46

Table S3. Electronic parameters of the HTLs extracted from UPS spectra.

Sample	E_{cutoff} **(eV)**	E_{onset} **(eV)**	E_F **(eV)**	E_g **(eV)**	**VBM (eV)**	**CBM (eV)**
NiO_x/Me-4PACz	0.88	16.55	-4.67	4.00	-5.55	-1.55
Laser NiO_x/Me-4PACz	0.92	16.47	-4.75	4.00	-5.67	-1.67

Table S4. Detailed photovoltaic parameters of the PSMs with different laser intensities.

Laser intensity	V_{OC} **(V)**	**FF (%)**	J_{SC} **(mA cm^{-2})**	**PCE (%)**
0 mJ cm^{-2}	12.38	76.13	2.17	20.46
16 mJ cm^{-2}	12.72	78.89	2.19	21.99
32 mJ cm^{-2}	12.85	79.30	2.23	22.70
48 mJ cm^{-2}	12.67	77.86	2.19	21.60

Table S5. Detailed photovoltaic parameters of the champion module, as well as the statistical data summarized from 15 PSMs from each group.

Sample	V_{OC} (V)	FF (%)	J_{SC} (mA cm^{-2})	PCE (%)	
Control	12.38	76.13	2.17	20.46	Highest
	12.29±0.09	73.31±1.61	2.16±0.01	19.55±0.55	Average
Target	12.85	79.30	2.23	22.70	Highest
	12.79±0.05	77.97±1.31	2.22±0.01	22.16±0.31	Average

Table S6. Comparison of the PCE of large-area PSMs fabricated through the blade-coating (active areas are 50-200 cm^2) in recent five years.

Device configuration	Active area (cm^2)	PCE (%)	Year	Ref
ITO/PTAA/Perovskite/C_{60}/BCP/Cu	50	19.2	2021	[9]
ITO/PTAA/Perovskite/C_{60}/BCP/Cu	60.8	16.3	2021	[10]
ITO/PTAA/Perovskite/C_{60}/BCP/Cu	53.6	18.9	2022	[11]
FTO/NiO_x/Perovskite/$PC_{61}BM$/BCP/Cu	174	18.6	2022	[12]
FTO/SnO_2/Perovskite/Spiro-OMeTAD/Au	100	17.7	2023	[13]
FTO/b-TiO_2/np-SnO_2/perovskite/Spiro-OMeTAD/Au	81	20.15	2023	[14]
ITO/PTAA/Perovskite/C_{60}/BCP/Cu	84	19.6	2024	[15]
ITO/PTAA/Perovskite/C_{60}/BCP/Cu	108	19.21	2024	[15]
FTO/NiO_x/Al_2O_3/SAM/Perovskite/C_{60}/BCP/Cr/Bi/Cu	113	20.14	2024	[16]
FTO/NiO_x/Perovskite/C_{60}/BCP/Cu	61.56	20.02	2025	[17]
FTO/NiO_x/SAM/Perovskite/C_{60}/BCP/Cu	57.3	20.6	2025	[18]
ITO/SnO_2/Perovskite/Spiro-OMeTAD/Au	57.2	22.76 (certified 21.6)	2025	[19]
FTO/NiO_x/SAM/Perovskite/C_{60}/BCP/Cu	**65**	**22.70 (certified 22.01)**	**2026**	**This work**

Table S7. Comparison of the PCE of small-area inverted PSCs using sputtered NiO_x films (active areas ≤ 1 cm^2) in recent five years.

Device configuration	Active area (cm^2)	PCE (%)	Year	Ref
ITO/sp-NiO_x/Perovskite/PCBM/AZO/Ag	1	15.6	2021	[20]
ITO/sp-NiO_x/Perovskite/PCBM/AZO/Ag	1	17.2	2022	[21]
ITO/sp-NiO_x/PTAA/Perovskite/PCBM/BCP/Ag	0.09	18.5	2022	[22]
ITO/sp-NiO_x/Perovskite/PCBM/BCP/Ag	0.04	19.1	2022	[23]
FTO/sp-NiO_x/Perovskite/PCBM/BCP/Ag	0.06	20.01	2023	[24]
ITO/sp-NiO_x/Perovskite/ZnO/PCBM/Ag	0.046	20.45	2023	[25]
ITO/sp-NiO_x/SAM/Perovskite/C_{60}/BCP/Ag	0.046	20.54	2024	[26]
ITO/sp-NiO_x/SAM/Perovskite/LiF/C_{60}/BCP/Ag	0.13	21.3	2024	[27]
FTO/sp-NiO_x/TFFA/Perovskite/C_{60}/BCP/Ag	0.049	22.76	2024	[28]
ITO/sp-NiO_x/Perovskite/PCBM/BCP/Ag	0.08	23.07	2025	[29]
ITO/sp-NiO_x/SAM/Perovskite/C_{60}/SnO_2/IZO/Ag	0.12	23.22	2025	[30]
FTO/sp-NiO_x/SAM/Perovskite/C_{60}/BCP/Ag	1.0	23.96	2025	[31]
FTO/NiO_x/SAM/Perovskite/C_{60}/BCP/Cu	**0.049**	**24.27**	**2026**	**This work**

References

1 G. Kresse and J. Furthmüller, Efficient iterative schemes for *ab initio* total-energy calculations using a plane-wave basis set, *Phys. Rev. B*, 1996, **54**, 11169.

2 G. Kresse and J. Furthmüller, Efficiency of ab-initio total energy calculations for metals and semiconductors using a plane-wave basis set, *Comput. Mater. Sci.*, 1996, **6**, 15-50.

3 P. E. Blöchl, Projector augmented-wave method, *Phys. Rev. B*, 1994, **50**, 17953.

4 J. P. Perdew, K. Burke and M. Ernzerhof, Generalized Gradient Approximation Made Simple, *Phys. Rev. Lett.*, 1996, **77**, 3865.

5 S. Grimme, J. Antony, S. Ehrlich and H. Krieg, A consistent and accurate ab initio parametrization of density functional dispersion correction (DFT-D) for the 94 elements H-Pu, *J. Chem. Phys.*, 2010, **132**, 154104.

6 F. Li, X. Deng, F. Qi, Z. Li, D. Liu, D. Shen, M. Qin, S. Wu, F. Lin, S. H. Jang, J. Zhang, X. Lu, D. Lei, C. S. Lee, Z. Zhu and A. K. -Y. Jen, Regulating Surface Termination for Efficient Inverted Perovskite Solar Cells with Greater Than 23% Efficiency, *J. Am. Chem. Soc.*, 2020, **142**, 20134-20142.

7 C. Luo, G. Zheng, F. Gao, X. Wang, C. Zhan, X. Gao and Q. Zhao, Engineering the buried interface in perovskite solar cells via lattice-matched electron transport layer, *Nat. Photonics*, 2023, **17**, 856-864.

8 W. Peng, K. Mao, F. Cai, H. Meng, Z. Zhu, T. Li, S. Yuan, Z. Xu, X. Feng, J. Xu, M. D. McGehee, J. Xu, Reducing nonradiative recombination in perovskite solar cells with a porous insulator contact, *Science*, 2023, **379**, 683-690.

9 S. Chen, X. Dai, S. Xu, H. Jiao, L. Zhao and J. Huang, Stabilizing perovskite-substrate interfaces for high-performance perovskite modules, *Science*, 2021, **373**, 902-907.

10 S. Chen, Y. Deng, X. Xiao, S. Xu, P. N. Rudd and J. Huang, Preventing lead leakage with built-in resin layers for sustainable perovskite solar cells, *Nat. Sustain.*, 2021, **4**, 636-643.

11 J. Yin, X. Shi, L. Wang, H. Yan and S. Chen, High-Performance Inverted Perovskite Solar Devices Enabled by a Polyfullerene Electron Transporting Material, *Angew. Chem. Int. Ed.*, 2022, **61**, e202210610.

12 M. Du, S. Zhao, L. Duan, Y. Cao, H. Wang, Y. Sun, L. Wang, X. Zhu, J. Feng, L. Liu, X. Jiang, Q. Dong, Y. Shi, K. Wang and S. Liu, Surface redox engineering of vacuum-deposited NiOx for top-performance perovskite solar cells and modules, *Joule*, 2022, **6**, 1931-1943.

13 R. Chen, Y. Yang, Z. Dai, L. Yuan, J. Du, P, Yang, Y. Yang, H. Shen, Z. Liu and H. Wang, Patch-healed grain boundary strategy to stabilize perovskite films for high-performance solar modules, *Nano Energy*, 2023, **115**, 108759.

14 J. Chung, S. -W. Kim, Y. Li, T. Mariam, X. Wang, M. Rajakaruna, M. M. Saeed, A. Abudulimu, S. S. Shin, K. N. Guye, Z. Huang, R. J. E. Westbrook, E. Miller, B. Subedi, N. J. Podraza, M. J. Heben, R. J. Ellingson, D. S. Ginger, Z. Song and Y. Yan, Engineering Perovskite Precursor Inks for Scalable Production of High-Efficiency Perovskite Photovoltaic Modules, *Adv. Energy Mater.*, 2023, **13**, 2300595.

15 M. A. Uddin, P. J. S. Rana, Z. Ni, G. Yang, M. Li, M. Wang, H. Gu, H. Zhang, B. D. Dou, J. Huang, Iodide manipulation using zinc additives for efficient perovskite solar minimodules, *Nat. Commun.*, 2024, **15**, 1355.

16 W. Liu, R. Chen, Z. Tan, J. Wang, S. Liu, C. Shi, X. Liu, Y. Cai, F. Ren, Z. Zhou, Q. Zhou, W. Li, T. Miao, H. Zhu, T. Imran, Z. Liu and W. Chen, Buried Interface Engineering for Scalable Processing of High-Performance Inverted Perovskite Solar Modules, *Adv. Energy Mater.*, 2025, **15**, 2404374.

17 J. Zhang , B. He, J. Huang, L. Yang, Y. Ding, W. Zhang, Y. Guo, L. Shi, A. Abudula, W. Du, X. Hao, X. Ji, Li. Yang, G. Guan, Lin. Lu, Z. Su and X. Gao, Regulating Crystallization Kinetics in High-performance Perovskites Solar Modules via Vapor Seed Layer Engineering, *Chem. Eng. J.*, 2025, **510**, 161632.

18 L. Wang, S. Yuan, F. Qian, T. Zhang, H. Zheng, X. Li, T. Lan, Q. Xu, P. Zhang and S. Li, Electrophilic molecule-induced π–π interactions reduce energy disorder of the hole transport layer for highly efficient perovskite solar modules, *Energy Environ. Sci.*, 2024, **17**, 8337-8348.

19 X. Zhu, D. Yu, X. Zhou, N. Wang, H. Liu, Z. Liang, C, Wu, K, Wang, D. Jin, S. Liu and D. Yang, Interfacial molecular anchor for ambient all-bladed perovskite solar modules, *Joule*, 2025, **9**, 101919.

20 N. Pant, A. Kulkarni, M. Yanagida, Y. Shirai, S. Yashiro, M. Sumiya, T. Miyasaka and K. Miyano, Passivation of Bulk and Interface Defects in Sputtered-NiO_x-Based Planar Perovskite Solar Cells: A Facile Interfacial Engineering Strategy with Alkali Metal Halide Salts, *ACS Appl. Energy Mater.*, 2021, **4**, 4530-454.

21 A. R. M. Alghamdi, M. Yanagida, Y. Shirai, G. G. Andersson and K. Miyano, Surface Passivation of Sputtered NiO_x Using a SAM Interface Layer to Enhance the Performance of Perovskite Solar Cells, *ACS Omega*, 2022, **7**, 12147-12157.

22 Y. Yang, J. Chen, C. Li, W. Zhang, S. -T. Zhang, D. Li, J. Zhang, Y, Ding, L. Lu and Y. Song,

Surface modified NiO_x as an efficient hole transport layer in inverted perovskite solar cells, *J. Mater. Sci.-Mater. Electron.*, 2022, **33**, 18522-18532.

23 W. Zhang, H. Shen, P. Yan and J. Zhang, Interfacial engineering of sputtered NiO_x for enhancing efficiency and stability of inverted perovskite solar cells, *Sol. Energy*, 2022, **248**, 128-136.

24 Z. Peng, Z. Zuo, Q. Qi, S. Hou, Y. Fu and D. Zou, Managing the Double-Edged Sword of Ni^{3+} in Sputter-Deposited NiO_x by Interfacial Redox Reactions for Efficient Perovskite Solar Cells, *ACS Appl. Energy Mater.*, 2023, **6**, 1396-1403.

25 D. S. Mann, S. -N. Kwon, P. Patil and S. -I. Na, Revivification of nickel oxide-perovskite interfaces via nickel nitrate to boost performance in perovskite solar cells, *Nano Energy*, 2023, **106**, 108062.

26 J. K. Kim, E. Cho, H. -J. Lee, S. -N. Kwon, J. -S. Park, M. Kim, D. H. Kim, S. -I. Na and S. -J. Lee, Enhancing Efficiency of Inverted Perovskite Solar Cells by Sputtered Nickel Oxide Hole-Transport Layers, *Solar RRL*, 2024, **8**, 2300933.

27 M. Tutundzic, X. Zhang, S. Lammar, S. Singh, P. Marchezi, T. Merckx, A. Aguirre, E. Moons, T. Aernouts, Y. Kuang and B. Vermang, Toward Efficient and Fully Scalable Sputtered NiO_x-Based Inverted Perovskite Solar Modules via Co-Ordinated Modification Strategies, *Solar RRL*, 2024, 8, 2300862.

28 Z. Lv, G. Liu, Z. Wang, Y. Gao, W. Lu, J. Wei, L. Zhang, P. Wang, Y. Yan, Y. Shi and J. Bian, Surface Property Regulation of a Magnetron-Sputtered NiO_x Hole Transport Layer for High-Performance Inverted Perovskite Solar Cells, *ACS Appl. Mater. Interfaces*, 2024, 16, 40, 54272-54281.

29 G. Ma, Q, Tan, Z. Li, J. Xiu, J. Wang, T. Cheng, D. He, Q. Sun, X. Ma, F. Lamberti and Z. He, Magnetron sputtered nickel oxide with suppressed interfacial defect states for efficient inverted perovskite solar cells, *J. Energy Chem.*, 2025, **100**, 348-355.

30 Y. Jin, H. Feng, Y. Li, H. Zhang, X. Chen, Y. Zhong, Q. Zeng, J. Huang, Y. Weng, J. Yang, C. Tian, J. Zhang, L. Xie and Z. Wei, Recrystallizing Sputtered NiOx for Improved Hole Extraction in Perovskite/Silicon Tandem Solar Cells, *Adv. Energy Mater.*, 2025, **15**, 2403911.

31 L. K. Lee, N. Li, X. Wang, H. Liang, J. Chen, R. Guo, Z. Dong, Z. Shi, T. Wang, D. Lai, S. Liu, Z. Jia, Y. Wang, X. Guo, J. Li, Q. Zhou, A. G. Aberle and Y. Hou, Oxygen-Dependent Sputtered NiO_x for High-Performance Perovskite Solar Cells and Minimodules, *ACS Mater. Lett.*, 2025, **7**, 1698-1706.